Analysis of a Computationally Simulated Three Stream Jet Flow for Noise Mitigation

Undergraduate Thesis

Presented in Partial Fulfillment of the Requirements for Graduation with Honors Research Distinction from the Department of Mechanical and Aerospace Engineering at The Ohio State University

by

Nick Salamon

May 2018

Advisor: Professor Datta Gaitonde

Committee: Professor Datta Gaitonde,
Professor John Horack

Abstract:

The energetic flow that emanates from a jet engine is what propels aircrafts to their destinations, but it is also the source of noise that is harmful to humans. Exposure to high levels of jet noise can cause acute symptoms like hearing loss and sleep disturbances, while prolonged exposure can significantly decrease a person's quality of life. Due to the ubiquity of commercial air transportation, the problem of jet noise and jet noise mitigation is an important area of research. It is believed that jet noise is caused by the process of turbulent mixing between slow ambient air and fast air coming from an aircraft engine. A proposed mitigation strategy aims to ease this turbulent transition. The solution involves the addition of a third stream of flow to the conventional dual stream turbofan engines. An additional layer of flow strategically placed between the bypass and ambient air could reduce turbulent noise generation. To assess this proposed solution, high-fidelity computational fluid dynamics (CFD) models have been simulated. In this paper, the data resulting from these simulations will be compared to experimental data and analyzed to determine the sonic characteristics of the flow from a three-stream engine.

Acknowledgements:

I would like to thank Professor Datta Gaitonde for advising me. His advice was readily available and without his patience and understanding, this project could never have been completed. I would also like to thank Professor Robert Siston for dedicating time to the 4999H class and giving very important feedback after my presentations. Dr. Kalyan Goparaju was also a great help. He spent time helping me understand all of the important tools I used for this project, for which I am grateful.

I would also like to thank my parents for supporting me in innumerable ways. Nothing I have accomplished could have happened without them.

Table of Contents:

Chapter 1: Introduction and Motivation

Aircraft noise is a serious public health issue. Because most airports are situated near densely populated urban areas, noise from takeoffs and landings affect a large number of people. 60 dB aircraft noise (comparable to the volume of a normal conversation) is audible as far as four miles from airports [1]. Short-term exposure can cause sleep disturbances, while longer exposure has been linked to higher rates of cardiovascular disease [2]. Aircraft noise is also an occupational hazard for people who have to work near airplanes in both civilian and military settings [3]. For these reasons, it is important to study aircraft noise and strategies for its mitigation. Because airlines must meet FAA regulations, aircraft noise is also a topic of interest for the aviation industry.

To understand potential noise reduction strategies, it is important to first understand the nature of sound and aircraft noise on a fundamental level. Sound, in the sense relevant to this discussion, consists of pressure waves that move through air or a gaseous medium. In all cases, sound represents a transferal of energy through a medium. This fact can help conceptually tie loud noises to "high-energy" events, and will be important for analyses later on. The sound generated by commercial aircraft can be further categorized by dividing it into its two main causes. The first type is caused when air is energized through interacting with the moving outer surface of the craft, and is aptly named "airframe noise". The second type of noise is "jet noise" which occurs when the high-energy exhaust from an engine mixes with low-energy ambient air. Most noise produced by commercial airplane operation is jet noise, so it stands to reason that aircraft noise mitigation strategies would focus primarily on reducing jet noise.

One of the main challenges in jet noise reduction is the fact that jet noise is fundamentally linked to the energy of engine exhaust flow, which is fundamentally linked to an airplane's the ability to stay in the sky. The connection between noise and exhaust flow can be understood through the acoustic analogies of Lighthill and other researchers [4,5]. These analogies point to structures generated in the region of flow between a jet and ambient air as the main sources of jet noise. This region is denoted the "shear layer" because of the high velocity gradient, which results in large viscous shear stresses compared to more uniform regions of a flow [6]. The instability in this transition region gives rise to turbulent structures that are thought to cause jet noise at various frequencies.

In a conventional turbofan engine, the turbulent structures mentioned above arise after flow passes through two separate sections of the engine. A turbofan engine is made up of a turbojet (gas turbine engine) and a fan that is driven by the energy produced by the turbojet. This configuration splits the incoming airflow into separate streams. The air that moves through the turbojet is the "core" stream, while the air that moves through the ducted fan section is the "bypass" stream. Combining a turbojet and a fan allows for a more fuel efficient engine in comparison to a turbojet alone, which is why the majority of commercial aircrafts are equipped with turbofan engines. Still, these engines produce an amount of noise that is problematic for regulatory bodies like the FAA and people who are exposed.

Proposed mitigation techniques and solutions to the problem of aircraft noise have approached the problem from several angles. As mentioned, governmental agencies have imposed regulations on operating volume. Noise can also be reduced in residential areas through

subsidized acoustic insulation and other hardware. Several efforts to directly reduce jet noise at its source have been studied. The approach of changing the physical geometry of the engine exit nozzle to passively promote quieter turbulent mixing is exemplified by the addition of chevrons or lobed nozzles [7]. The use of plasma actuators has been another approach that seeks to actively influence the sonic characteristics of jet flows by strategically exciting regions of the flow [8].

Another proposed solution is the addition of a third stream of flow to the conventional dual-stream turbofan engines used today. The third stream would be placed between the ambient air and the bypass stream. This has the potential to decrease the turbulence of the fluid mixing between the high-speed core flow and the low-speed ambient air. Reducing the turbulence associated with this mixing could decrease the amount of noise created by the engine exit flow. Henderson has done research involving experimental studies on the flow characteristics of three-stream jets [9]. Recent CFD simulations carried out by Dr. Datta Gaitonde and the High-Fidelity Computational Multi-Physics Lab at the Ohio State University have recreated some of Henderson's experiments. The simulations analyzed in this paper are those that model Henderson’s axisymmetric three-stream flows. Post processing and analysis was done on two of these models. The results are presented in this paper.

Chapter 2: Problem Details

The data analyzed here were calculated in high-fidelity CFD simulations. The three-dimensional mesh that was used had millions of cells, of which cross-sections are shown in figure 1. The fully white areas are where the resolution of the mesh is too fine to be captured by the software at the display magnification. The grid was constructed in a cylindrical coordinate system. The I coordinate is positive to the right, the J coordinate is equivalent to the radius (distance from centerline), and the K component is the angle. In solving the governing equations of the flow in each cell in the domain, the model approximates the true physics of the three-stream jet. Furthermore, the numerical nature of CFD modeling means that gathering data is faster and more direct than in experimental analyses.

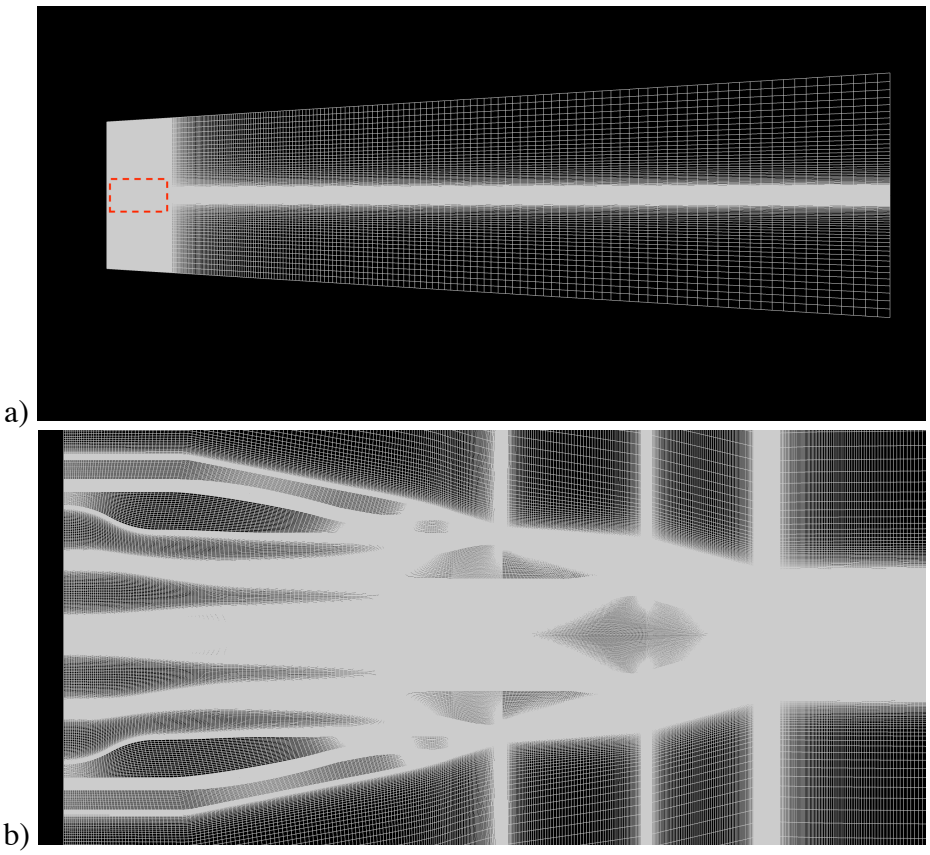

Figure 1: Mesh used to simulate axisymmetric three-stream nozzle. a) shows one “slice” of the entire computational

domain. b) shows a closer view of the nozzle region of the mesh, shown in a) as the area enclosed by the rectangle.

The primary simulation considered here is the axisymmetric heated three-stream jet with co-flow. Co-flow refers to the condition of an ambient that is moving with some given velocity. In this case, the co-flow moves at Mach 0.3 in the direction of the jet motion. The secondary simulation that was also considered was a case without co-flow, in which the ambient air was initially stagnant and unperturbed.

All values in the simulated dataset have been nondimensionalized. Variables without units allows for an easier comparison to Henderson's data, which is also nondimensionalized. Additionally, nondimensionalization allows the results to be scaled easily. The variables output by the CFD solver are pressure, density, and velocity. These variables are nondimensionalized by multiplying or dividing by values characteristic to the flow. The values used are 0.164 m, 347.188 m/s, and 1.1768 kg/m^3. Pressure is calculated from $P = \rho V^2 = 141850\ Pa$. Table 1 shows the pressure and temperature ratios used in both models. The temperature ratio is the ratio of the stream temperature to the ambient temperature. Likewise, the pressure ratio is the ratio of the stream "tank" pressure to the ambient pressure. The exit areas of the streams are equal.

Table 1: Nozzle operating conditions

Stream	Pressure Ratio	Temperature Ratio
Core	1.8	3
Bypass	1.8	1.25
Tertiary	2.1	1.25

Two types of simulated data were considered: mean flow data and transient flow data. As the name suggests, the mean flow data are the average values over the length of the simulation. The

output of this averaging was a full three-dimensional mesh with average values for each cell. The mean flow data has no time dependence and is thus a static "snapshot" that represents the average flow over time. Transient flow data has time dependence, which is necessary for the methods of analysis discussed in chapter 3. The primary sources of transient data were point probes. Because it would have been impractical or impossible to store transient data for the whole domain, these probes saved resources by taking data at several defined points. Figure 2 shows the locations of these points. The probes recorded all flow variables at every time step for a single point. A full list of the point probes, with their respective grid addresses and XYZ coordinates, can be found in appendix D. A secondary source of transient data was movie files. These less detailed files were used to visually display the transient data with flipbook-type movies.

The point probe files were given names of the format "LIPX_Y" where X is an integer from 1 to 3, and Y is an integer from 1 to 8. "LIP" was used because each of the three nozzle lips has a series of point probes associated with it. Lip 1 is the lip of the core stream nozzle exit, lip 2 is the lip of the bypass stream nozzle exit, and lip 3 corresponds to the tertiary stream. The lip files were all placed on the same K plane. LIP files that share an "X" address are all part of the same series, and all share a J coordinate. LIP files that share a "Y" address are grouped together, in that they share an I coordinate. This can be seen in figure 2, in which there are five groupings of three point probes, and two groupings of two probes. Only LIP3_1 has a unique I coordinate.

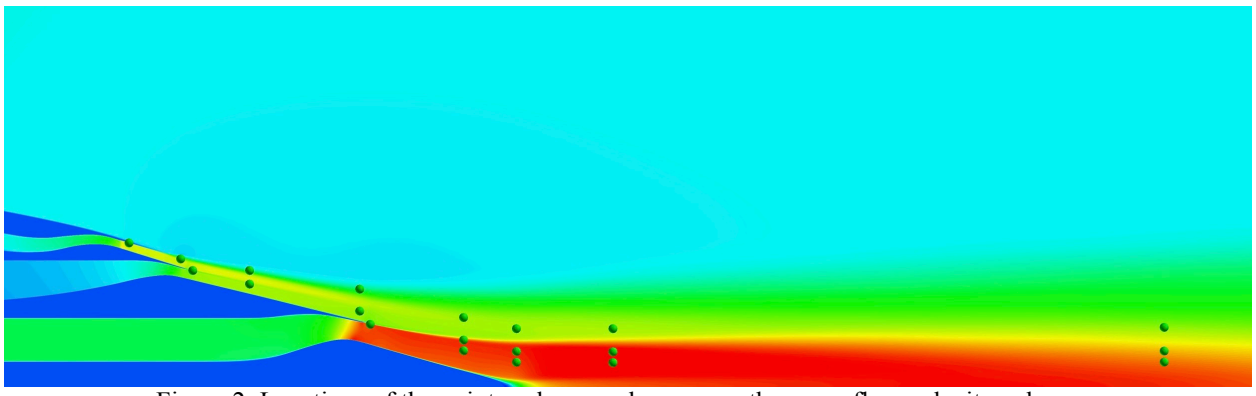

Figure 2: Locations of the point probes are shown over the mean flow velocity colormap

Chapter 3: Methods of Analysis

The flow was visualized using FieldView, which is a flexible software specifically designed for CFD visualization and post-processing. For this dataset, FieldView was used to create still images of the mean flow values in the simulated domain as well as a movie of the flow. The still images were taken at an arbitrary slice of the flow. This method is representative because the flow is axisymmetric. The movie was created by combining several "frames" which were output by the CFD solver. These frames are snapshots of the flow at different time values, with each frame containing information on all flow variables. FieldView was also used to display the cells of the 3D grid that served as the domain of the flow for the purpose of CFD simulation.

After visualization, the simulated flow was compared to Henderson's experiments. Although the flow data from the CFD simulation was already in a digital format, the data from Henderson's paper was presented only graphically. This necessitated the use of a plot digitizer. To extract data arrays from Henderson's plots, an online plot digitizer was used, which can be found here. In this process, a picture of a plot was uploaded and relevant points were manually entered using a cursor. While this "by-hand" method is a likely source of error, the error should be relatively small because of the accuracy allowed by the digitization software's zoom feature. The digitized plots should thus provide a good approximation for this initial comparison.

Next, MATLAB was used to compare the data for different areas of flow. Some of Henderson's data were nondimensionalized by different variables than those used for the CFD simulations [9]. Before creating comparison plots, the CFD data had to be nondimensionalized using values that corresponded to those used by Henderson. This was done by multiplying the relevant array of

values (pressure, velocity, etc.) by its respective nondimensionalization factor, which resulted in unitless data that could be compared to Henderson's plots. MATLAB was used to make comparison plots with Henderson's data and the CFD three-stream data on the same graph.

To analyze the sonic characteristics of the signals collected by point probes, three separate methods were implemented through MATLAB: fast Fourier transforms (FFT), short time Fourier transforms (STFT), and wavelet transforms. These tools give information about the distribution of frequencies in a uniformly sampled set of data points. In the case of pressure data from point probes, these tools are useful for determining the prevalence of various frequencies present in the pressure fluctuations at a point.

A fast Fourier transform computes the spectral density of data collected over a period of time. FFT includes any one of several algorithms that computes a discrete Fourier transform (DFT) in O(NlogN) computations as oppose to O(N^2) [10]. The smaller number of calculations means a FFT can give all the information much faster than a DFT, hence the name. The FFT gives important information about the frequencies present in a given time domain and their prevalence. The disadvantage of a FFT is that it does not give any information about *when* frequencies occur. This can be a problem when there are significant transients or unique events occurring in a flow.

The next method, the short time Fourier transform, attempts to solve the time resolution problem encountered with FFTs. It does this by splitting the time domain into equally spaced portions, and then running FFTs on each chunk of data in a given range of time [11]. Doing so gives information about what frequencies occur at what times. There is a trade off in that the sampling

window is decreased, so a STFT cannot capture all the frequencies that a full FFT can, though this may not be a problem if low frequencies are less important in a signal. A similar trade-off that is inherent to the STFT is that dividing point probe data into smaller time chunks will decrease the frequencies that can be observed, while larger time chunks will decrease the temporal resolution, meaning there will be less certainty of when frequencies occur.

The wavelet transform is similar to the STFT in that its output contains both time and frequency resolution. However, it uses a different method than the STFT. The wavelet transform is so named because it uses one "mother wavelet" to determine the frequencies that occur in a dataset. The mother wavelet is a constructed waveform of finite length, which is correlated to raw data. Because of its somewhat arbitrary nature, there are many different mother wavelets to choose from when performing a wavelet transform [12]. The basic operating principle for the method of wavelets is that the wavelet in its base form is correlated to the raw data section by section, according to the wavelet's length. When this "first pass" is completed, the wavelet is stretched and repeats the process until further stretching would exceed the length of the data.

For each of these methods of spectral analysis, data was imported to MATLAB before built-in MATLAB functions were executed for each respective algorithm. The transformed data was plotted using MATLAB.

Chapter 4: Results

4.1 Visualization

In visualizing the data, still images of the mean flow variables were created. Colormap images of the full domain are shown in figure 3. These pictures give an idea of the average flow values over the entire domain for the duration of the simulation. The pressure shown in figure 3a appears to be mostly uniform. The u velocity shown in figure 3b shows high velocity flow near the exit that steadily decreases with distance from the nozzle, as expected. Figure 3c shows lower density near the exit that steadily increases with distance, also as expected. An unexpected result is the low values found along the centerline in the right of Figures 3b and 3c for velocity and density, respectively. This may be due to the fact that the grid in this region is too fine. The pressure shown in figure 3a may not have experienced this discontinuity because pressure in this region simply stayed at the given ambient condition.

a)

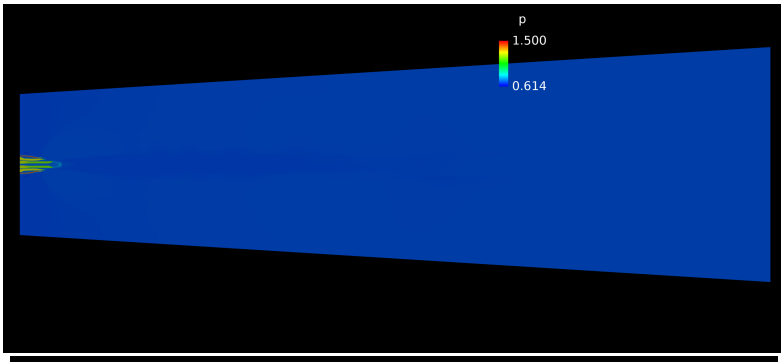

b)

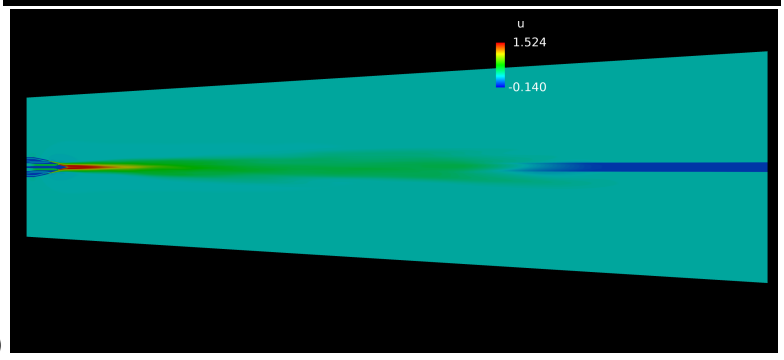

c) 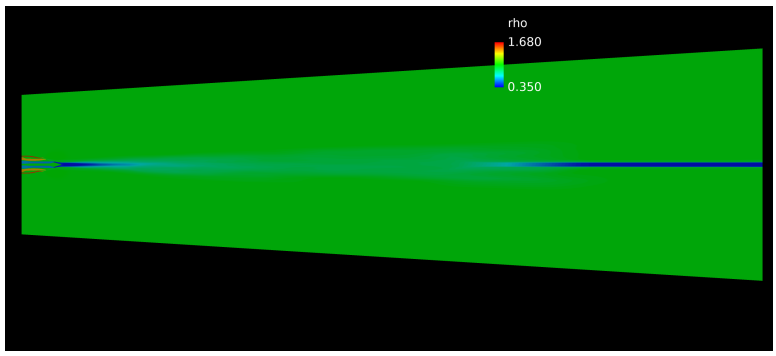

Figure 3: Full domain colormaps of the simulated flow. a) pressure b) u velocity c) density

Figure 4 gives a more detailed view of the nozzle region of the simulation. These images help confirm that the temperature and pressure ratio values listed in table 1 reflect the simulation. The highest pressure is found in the tertiary stream, with the core and bypass being similar in pressure. Because the core stream has a high temperature ratio of 3, compared to the bypass and tertiary temperature ratios of 1.25 each, there is lower pressure in the core stream than in the bypass stream. The supersonic flow exiting the core stream is indicated in figure 4b by the quick transition from green to red at the nozzle throat, and in figure 4a by the exit pressure higher than ambient pressure directly after the nozzle exit (shown as a light blue region around the nozzle spike). The failure to expand to ambient pressure indicates overexpanded flow, which is characteristic of some supersonic jets.

a) 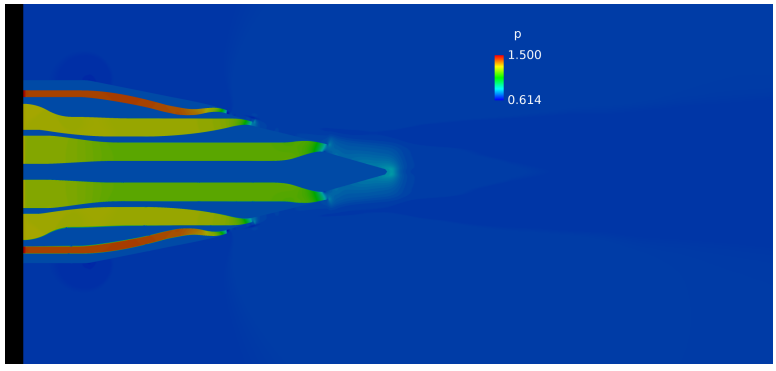

b)

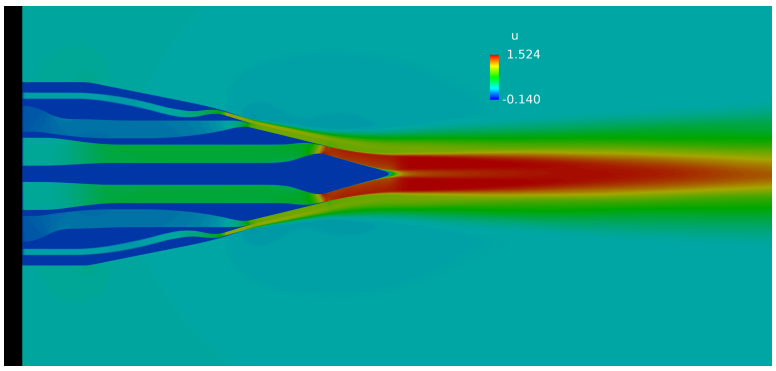

c)

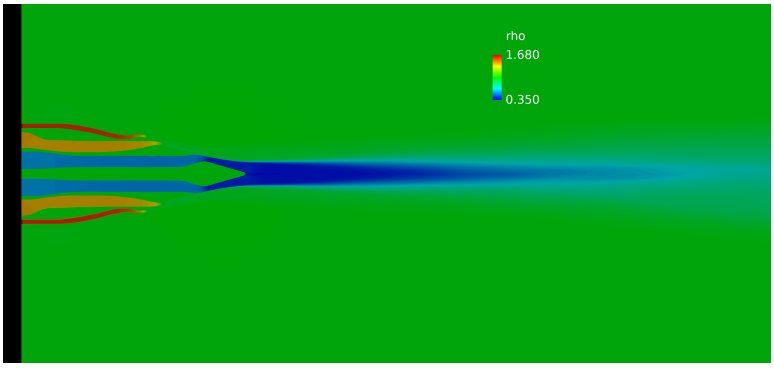

Figure 4: Coloramap images of flow variables near the nozzle. a) pressure b) u velocity c) density

In addition to still images of the mean flow, several videos were created to show the time-dependent flow behavior. Figure 5 shows a frame from one such video. In this movie, the variation in u velocity is played over a portion of the full time domain. The green dots represent point probe locations. They are present to give an understanding of how the flow variables change over specified points in the flow. Above the green region of the flow in figure 5 are what appear to be regular variations in velocity. These also appear in the movies that show the variation of pressure.

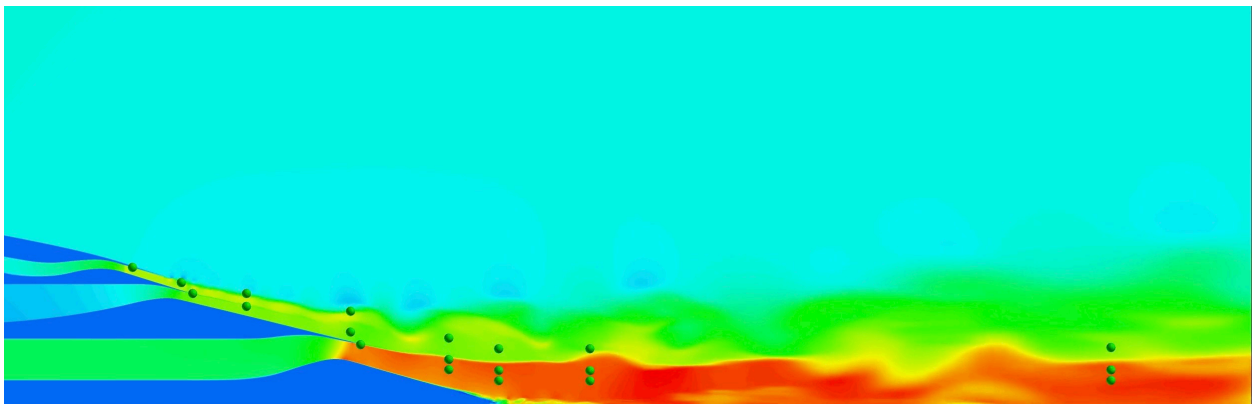

Figure 5: A frame from a video of u velocity. The green dots represent locations where point probe data were collected.

4.2 Comparison to Henderson's Data

Three of Henderson's plots displayed data for the axisymmetric, three-stream flow. These plots are used as a basis of comparison between Henderson's experiments and the simulated flows. After extracting data from the graphs using a plot digitizer, they were compared to the simulations using MATLAB. The results are shown in figures 6, 8, and 9.

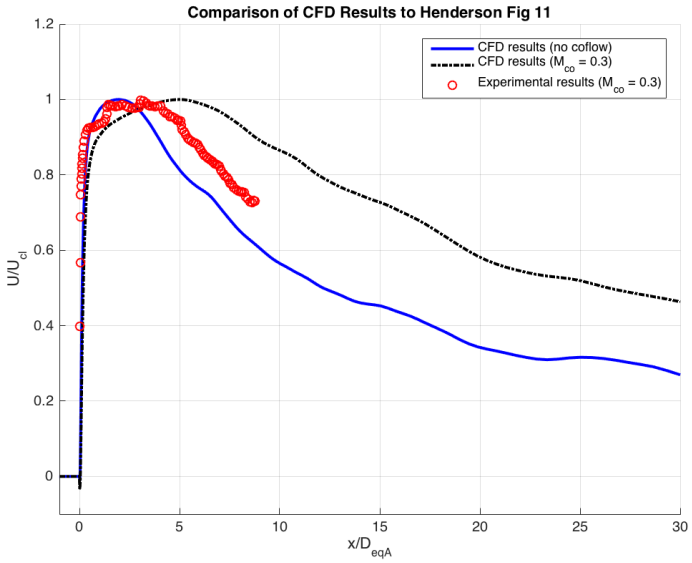

Figure 6: Plot comparing the centerline velocity of three flows

Figure 6 is a plot of centerline velocity versus distance from the nozzle tip. The maximum centerline velocity (U_{cl}) is used to normalize the velocity. This value was different for each of the three flows graphed, because maximum centerline velocity is a value characteristic to a specific

flow. The distance from the nozzle tip was normalized by the diameter for a circle with area equivalent to the total nozzle exit area for all three exits (D_{eqA}). This value was the same for each flow, because each flow used the same nozzle geometry. The black and blue lines represent CFD results with and without co-flow, respectively. The black line representing CFD results with co-flow stays higher than the blue line because of the Mach 0.3 co-flow in the simulated domain.

Though these plots are visually similar, there does seem to be a discrepancy between the experiment with co-flow and the simulation with co-flow. The velocity in the experimental results decreases much faster than it does in the computational results. This may be because Henderson's Nozzle Acoustic Test Rig (NATR) only allows for a region of co-flow around the nozzle of about three nozzle diameters. The CFD data were produced with a "full" co-flow, meaning the all the ambient air was moving at Mach 0.3 as defined by the simulation parameters. The diameter of the simulation section comparable to Henderson's NATR was around six nozzle diameters [9]. Figure 7 shows a comparison of the two test geometries.

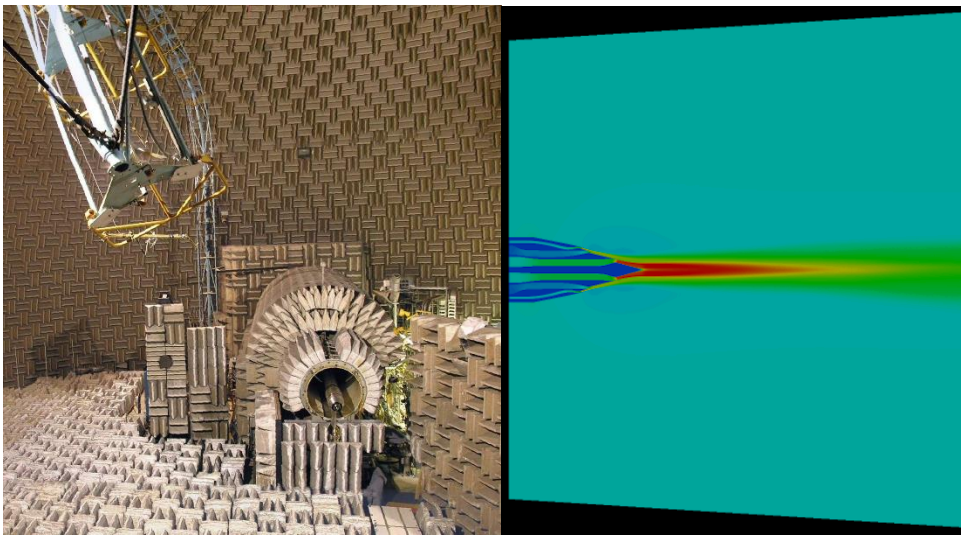

Figure 7: Comparison of test domains. The image on the left is Henderson's experimental setup with the NATR and nozzle visible in the lower right corner. The image on the right is the simulated nozzle with the width of the domain visible.

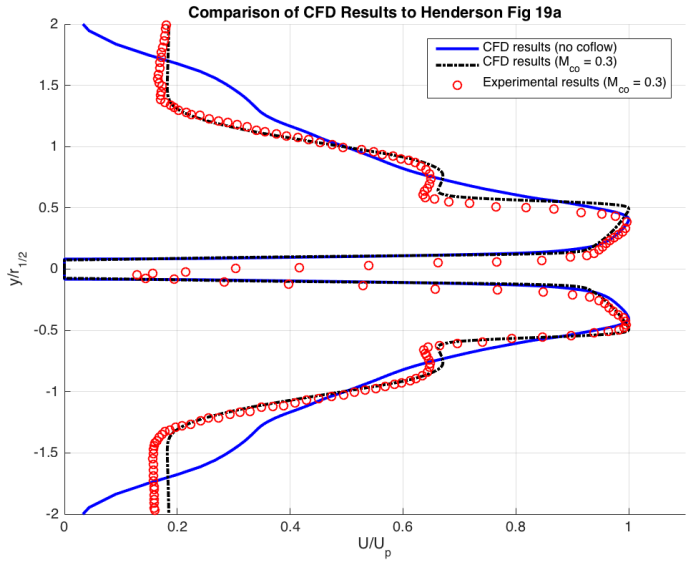

Figure 8: Plot comparing the K-plane velocity of three flows near the nozzle exit

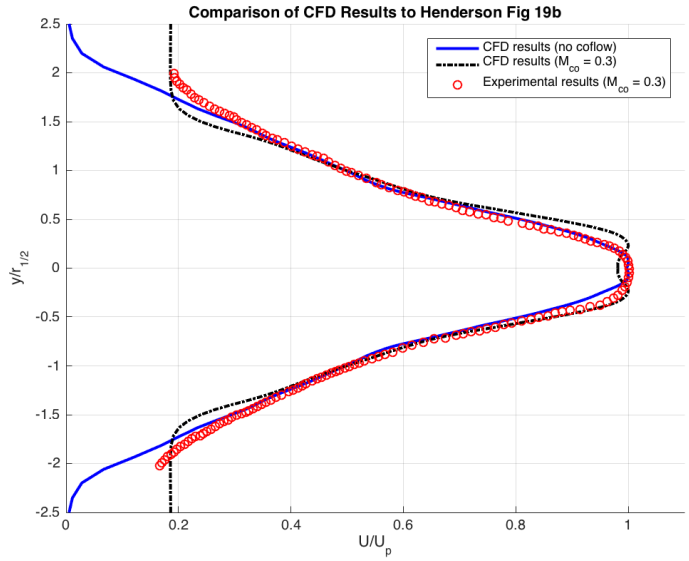

Figure 9: Plot comparing the K-plane velocity of three flows downstream of the nozzle exit

Figures 8 and 9 show graphs of the velocities along two sections of the K-plane (perpendicular to the flow). The axes are distance from the centerline versus velocity. The distance from the centerline is normalized using the half velocity radius ($r_{1/2}$), or the radius at which the flow velocity has decreased to half its peak value. The velocity is normalized by the peak value in the section (U_p). Figure 8 is a slice taken at an X coordinate close to the nozzle, while Figure 9 is at a

slice further downstream. Both of these graphs show good agreement between the experimental and computational results. This result serves to show that the simulation is a good approximation of the actual flow profile.

4.3 Frequency Analysis

FFT, STFT, and Wavelet were carried out on each point probe. Appendix A contains all the graphs of sound pressure level versus Strouhal number calculated by FFT. Appendix B contains all the spectrograms and scalograms calculated by STFT and Wavelet transform, respectively. Because FFT was run over the entire time domain, it was able to capture the majority of frequencies present. Many of the point probes captured resonant frequencies. Figure 10 is an example of this. Taken from the FFT data of LIP1_4, this detail plot clearly shows that each "spike" in the graph corresponds to a frequency that is simply an integer multiple of the first and largest spike. The first spike has a Strouhal number of 20, the next spike is 40, the next is 60, and so on. This indicates that most of the "shape" of this SPL profile is caused by a single flow event.

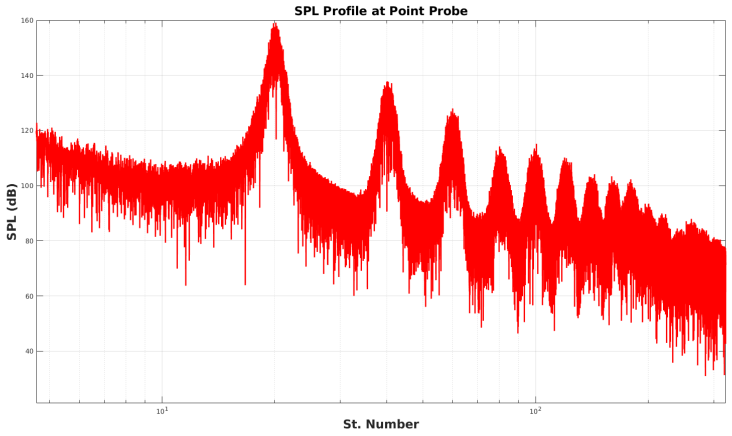

Figure 10: Detail of LIP1_4 SPL profile showing resonant frequency

The point probe LIP1_4 is also part of a group of three probes that share the same I coordinate. The other two probes are LIP2_4 and LIP3_4. As mentioned in Chapter 2, there are five such

groups. These groups show similar distributions and intensities of spectral frequencies, with differences that can be attributed to variable distance from the center core (J direction). This is confirmed by viewing the SPL profiles for each grouping. For each grouping, the graphs maintain spikes in frequency, but the dB measure increases from the innermost probe to the outermost probe. An example of this is shown in Figure 11. All three plots have a series of peak frequencies around a Strouhal number of 1. The max SPL in figure 11a is around 160 dB, the max in figure 11b is around 170 dB, and the max in figure 11c is around 180 dB. The difference in SPL between members of a group decreased with distance from the nozzle tip.

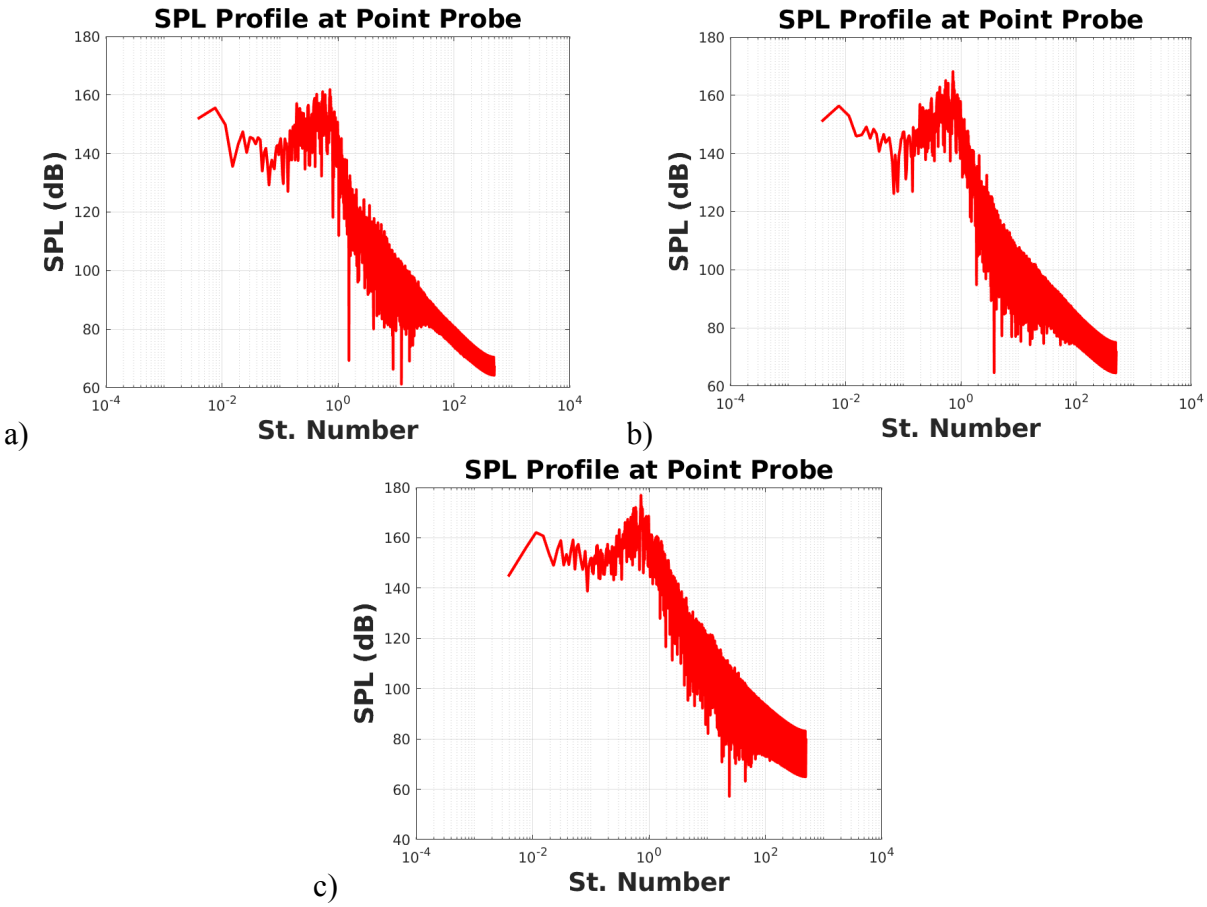

Figure 11: SPL plots for a grouping of point probes. a) LIP1_5: probe closest to centerline b) LIP2_5: middle probe c) LIP3_5: outermost probe

STFTs and Wavelet transforms were used to give an idea of any transient events occurring in the flow. In general, the results from STFT and Wavelet agreed with each other, as shown in figure 12. Both wavelet and STFT show basically the same frequencies appearing at the same times, though the wavelet transform results are less blocky and more precise in appearance.

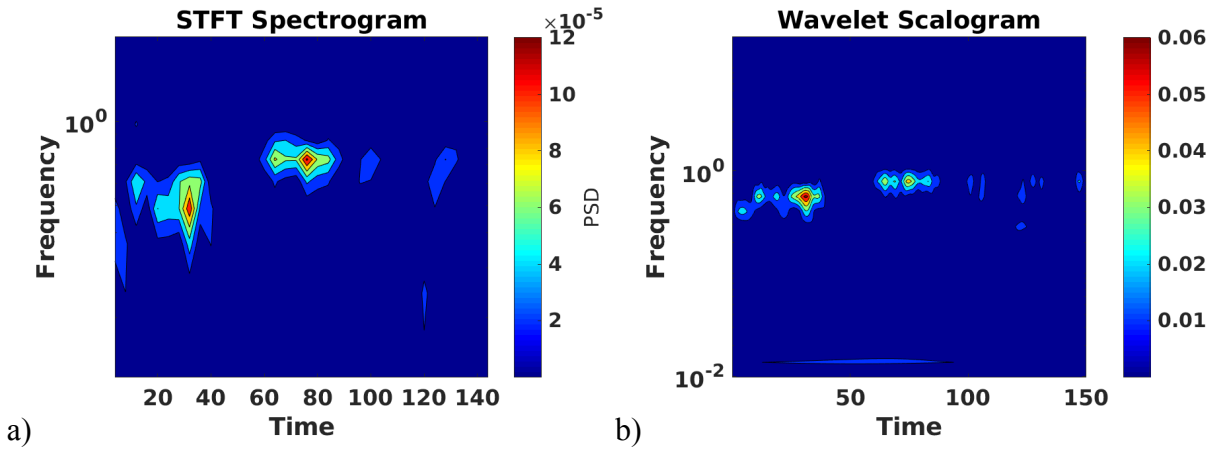

Figure 12: Results from STFT and Wavelet transform for LIP1_4

Both wavelet and STFT also picked up a transient event that occurs in the first third of the simulation. Figure 13 shows how around t = 50, the dominant frequencies shift from being clustered around a Strouhal number of 0.5 to a Strouhal number of 0.8. This shift can be observed in several of the STFT and wavelet results in Appendix B. Because the simulation is primarily operating at steady state, this is an unexpected result. In videos created over the entire time domain, there does seem to be a discontinuity around the time of the shift as seen in the STFT/Wavelet plots. Before and after the shift around t = 50, the frequencies seem to be steadily concentrated around fixed values, indicating steady state operation. Other STFT/Wavelet plots show a clear shift that does not necessarily share the same frequencies as those found in figure 13.

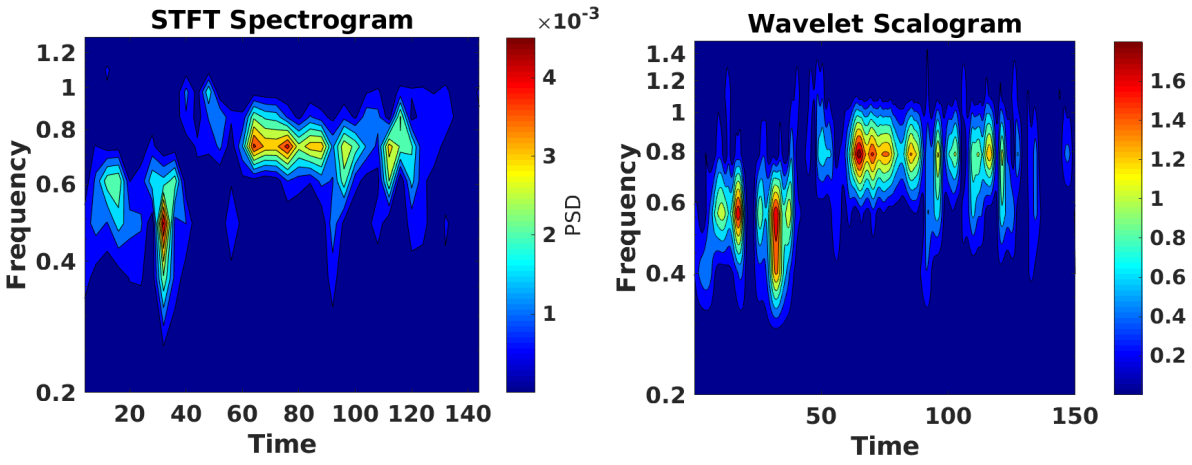

Figure 13: STFT and wavelet plots showing shift in frequency in early part of time domain

Chapter 5: Conclusions

This work has been done to post-process the data produced in a high-fidelity CFD simulation of three-stream jet flow. The data were visualized using still images and movies. The simulated data were compared to experimental data and found to be mostly in agreement. The disagreement seen in figure 6 can likely be explained by pointing out geometrical differences between Henderson's experiments and the simulation. Each point probe was analyzed using FFTs, STFTs, and wavelet transforms. These methods picked out the key frequencies within the flow, which all occurred around a Strouhal number of 1. The use of STFT and wavelet transforms also picked up an abrupt shift in steady state behavior, with an unknown cause.

The primary limitation of this analysis is that the point probes were all placed very close to the nozzle and core flow. Because of this, there was no way to determine far-field noise behavior using the methods listed. It follows that future research would use methods such as Ffowcs Williams-Hawkings (FWH) to get an idea of far-field noise that would be projected by the three-stream flow.

References

[1] Boston Logan Airport Noise Contours, Accessed March 2018 http://www.massport.com/logan-airport/about-logan/noise-abatement/contours/

[2] Correia, A. W., Peters, J. L., Levy, J. I., Melly, S., & Dominici, F. (2013). Residential exposure to aircraft noise and hospital admissions for cardiovascular diseases: multi-airport retrospective study. *bmj*, *347*, f5561.

[3] Yankaskas, K. (2013). Prelude: noise-induced tinnitus and hearing loss in the military. *Hearing research*, *295*, 3-8.

[4] Goldstein, M. E. (1976). Aeroacoustics. *New York, McGraw-Hill International Book Co., 1976. 305 p.*

[5] Lighthill, M. J. (1952). On sound generated aerodynamically I. General theory. *Proc. R. Soc. Lond. A*, *211*(1107), 564-587.

[6] Moore, C. J. (1977). The role of shear-layer instability waves in jet exhaust noise. *Journal of Fluid Mechanics*, *80*(2), 321-367.

[7] Callender, B., Gutmark, E. J., & Martens, S. (2005). Far-field acoustic investigation into chevron nozzle mechanisms and trends. *AIAA journal*, *43*(1), 87-95.

[8] Samimy, M., Kim, J. H., Kastner, J., Adamovich, I., & Utkin, Y. (2007). Active control of a Mach 0.9 jet for noise mitigation using plasma actuators. *AIAA journal*, *45*(4), 890-901.

[9] Henderson, B. S., & Wernet, M. (2016). Characterization of Three-Stream Jet Flow Fields. In *54th AIAA Aerospace Sciences Meeting* (p. 1636).

[10] Brigham, E. O., & Brigham, E. O. (1988). *The fast Fourier transform and its applications* (Vol. 1). Englewood Cliffs, NJ: prentice Hall.

[11] Welch, P. (1967). The use of fast Fourier transform for the estimation of power spectra: a method based on time averaging over short, modified periodograms. *IEEE Transactions on audio and electroacoustics*, *15*(2), 70-73.

[12] Graps, A. (1995). An introduction to wavelets. *IEEE computational science and engineering*, *2*(2), 50-61.

Appendix A (FFT results)

LIP1_4:

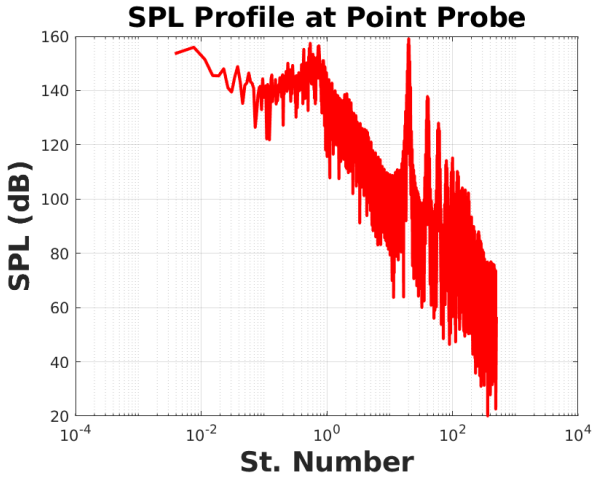

LIP1_5:

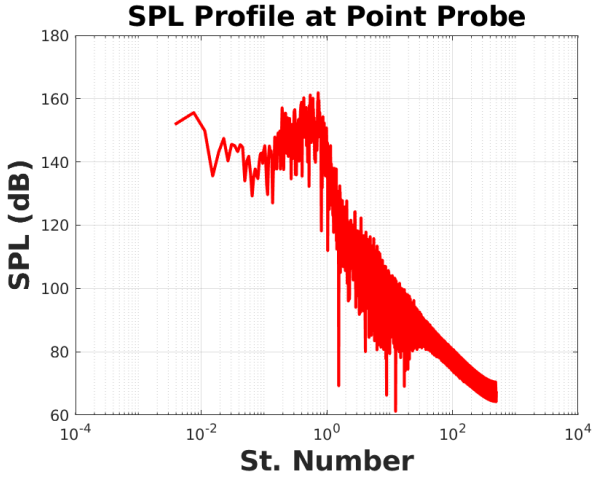

LIP1_6:

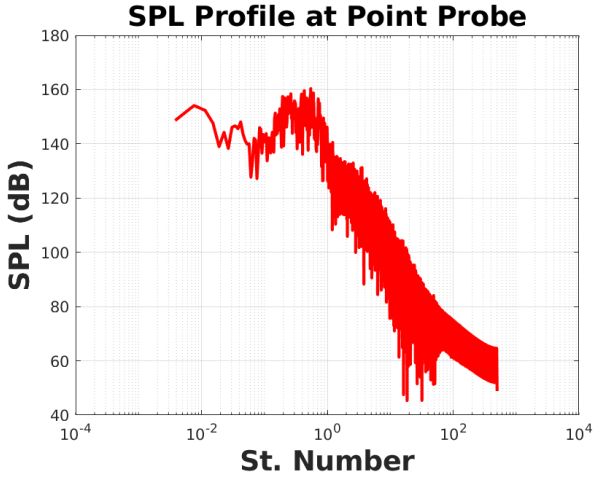

LIP1_7:

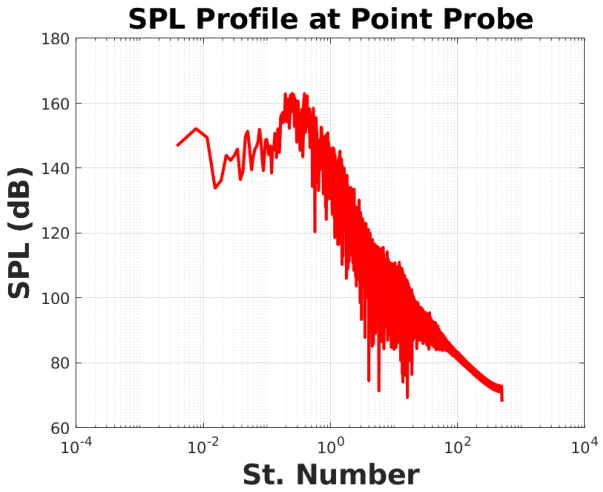

LIP1_8:

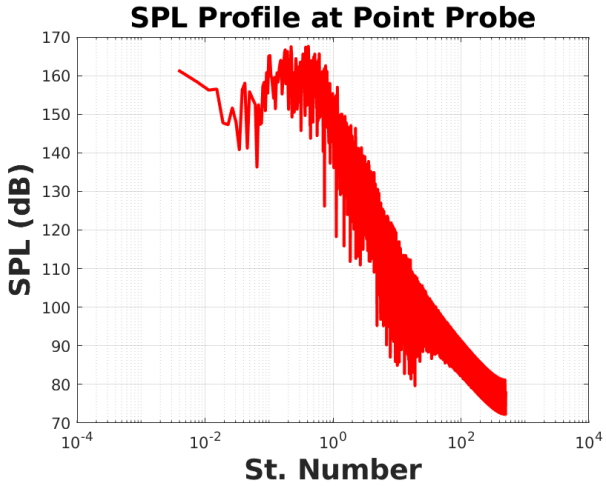

LIP2_2:

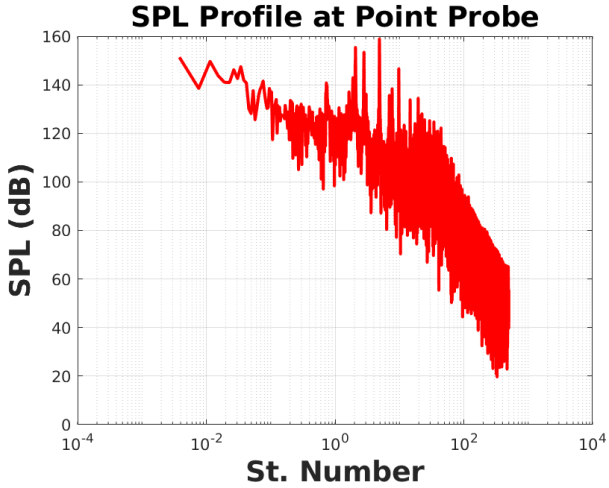

LIP2_3:

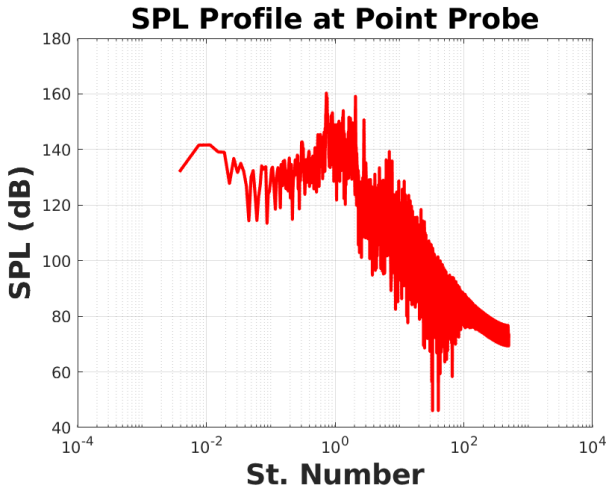

LIP2_4:

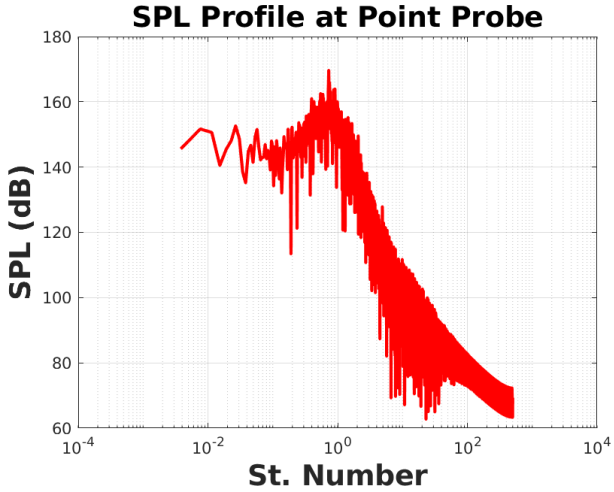

LIP2_5:

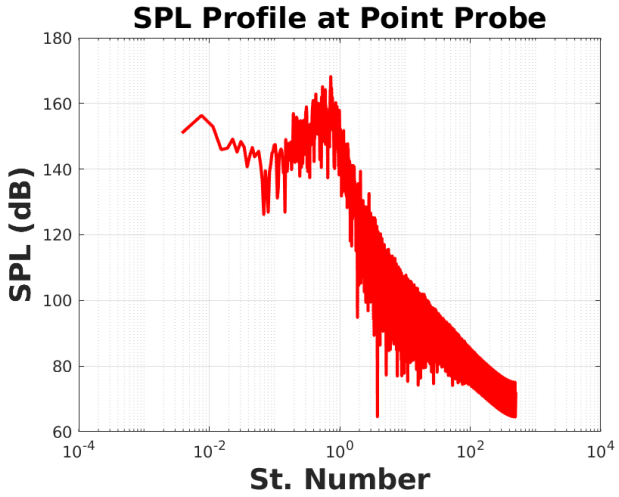

LIP2_6:

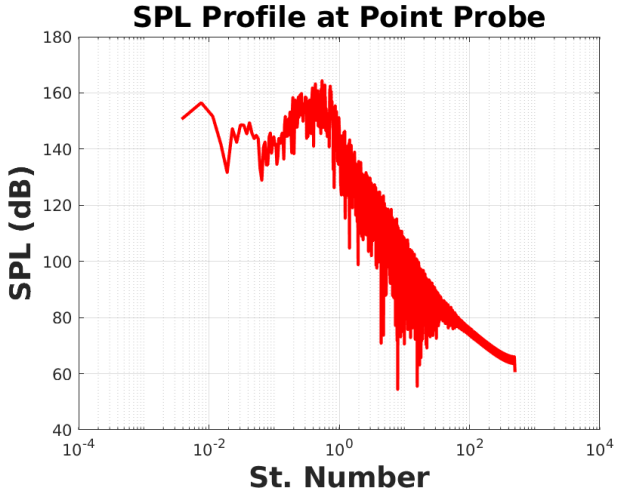

LIP2_7:

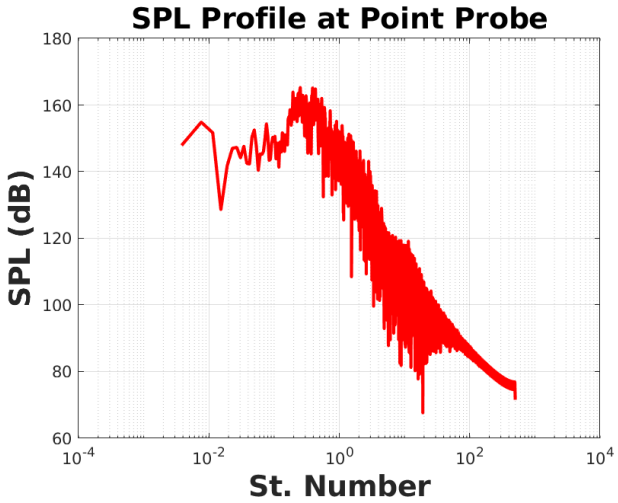

LIP2_8:

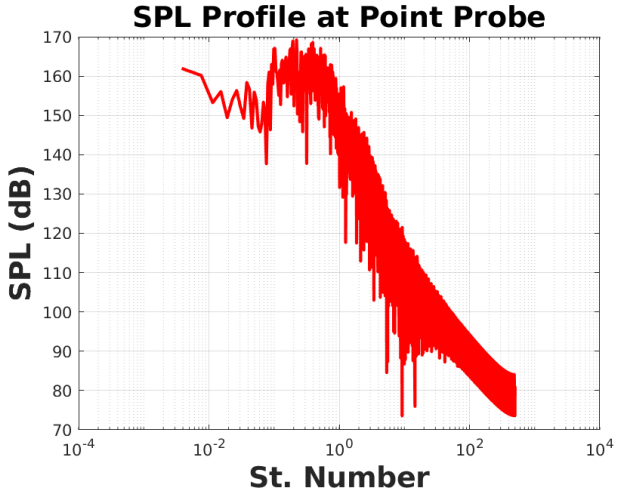

LIP3_1:

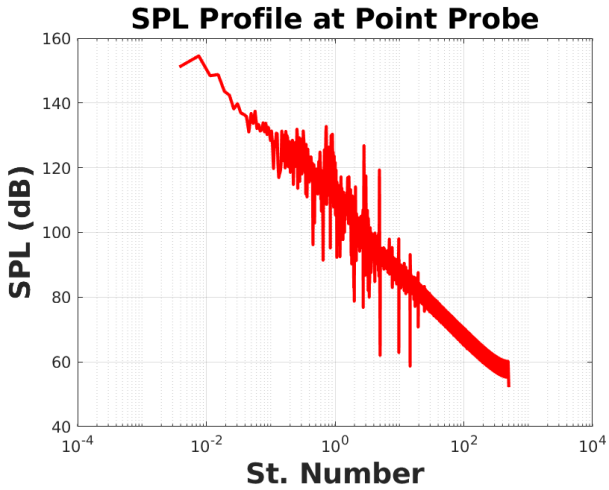

LIP3_2:

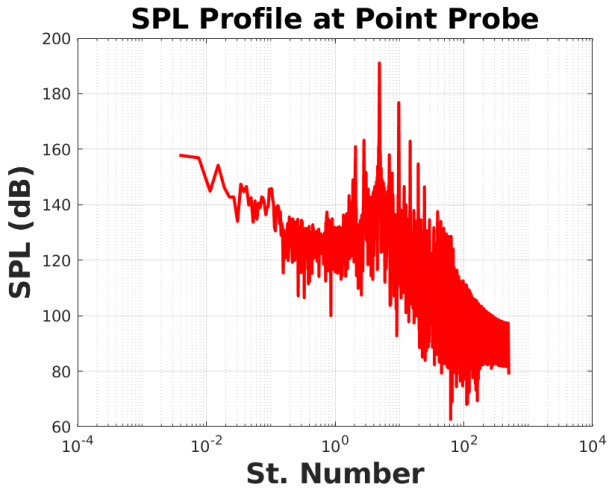

LIP3_3:

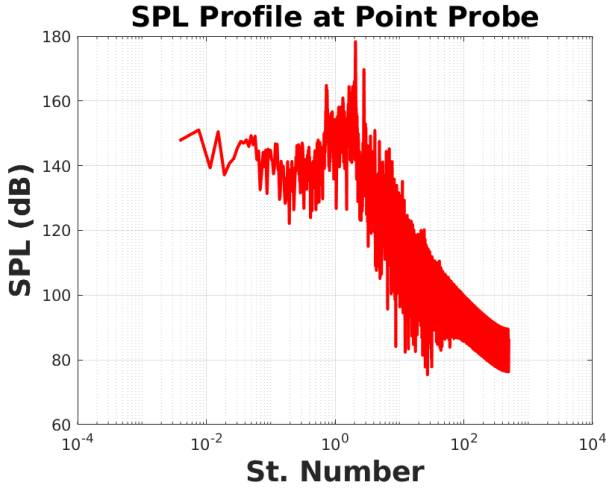

LIP3_4:

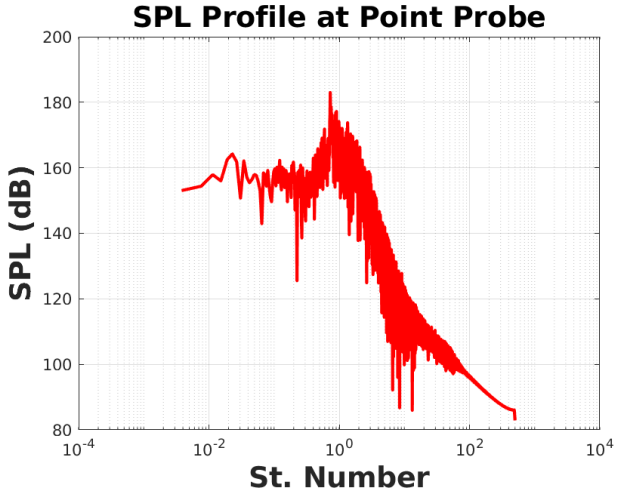

LIP3_5:

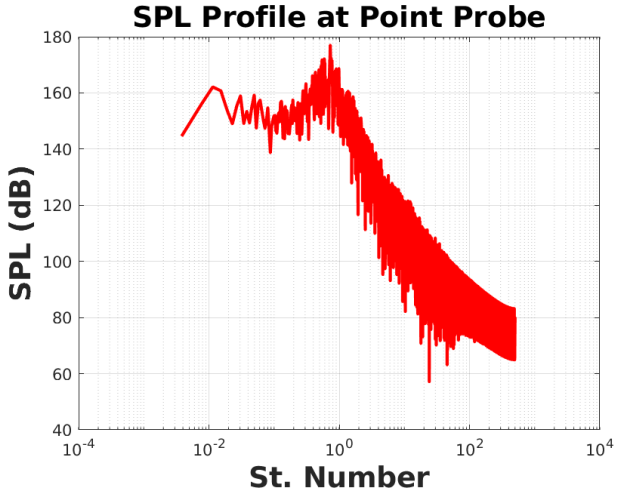

LIP3_6:

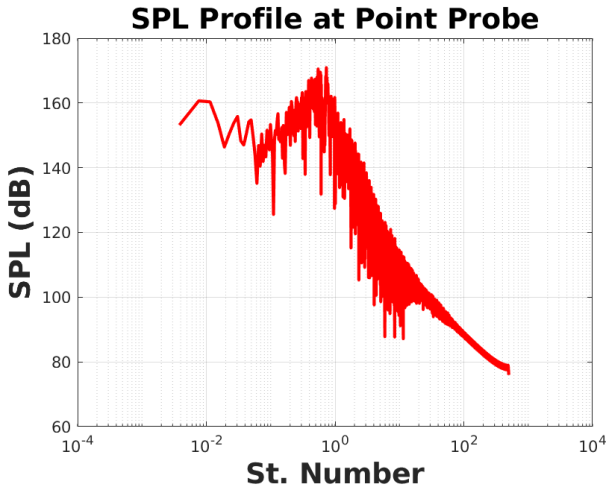

LIP3_7:

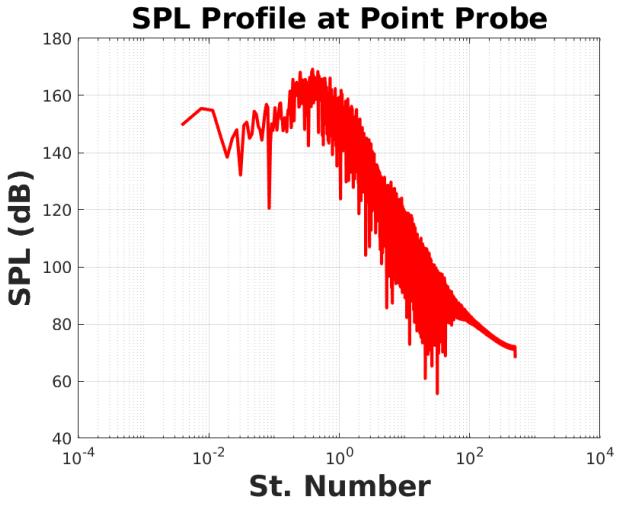
SPL Profile at Point Probe
SPL (dB)
St. Number
180
160
140
120
100
80
60
40
10^-4
10^-2
10^0
10^2
10^4

LIP3_8:

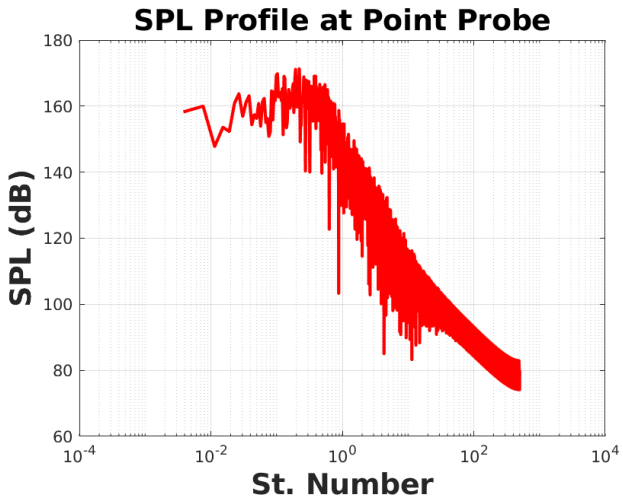
SPL Profile at Point Probe
SPL (dB)
St. Number
180
160
140
120
100
80
60
10^-4
10^-2
10^0
10^2
10^4

Appendix B (STFT and wavelet results)

LIP1_4:

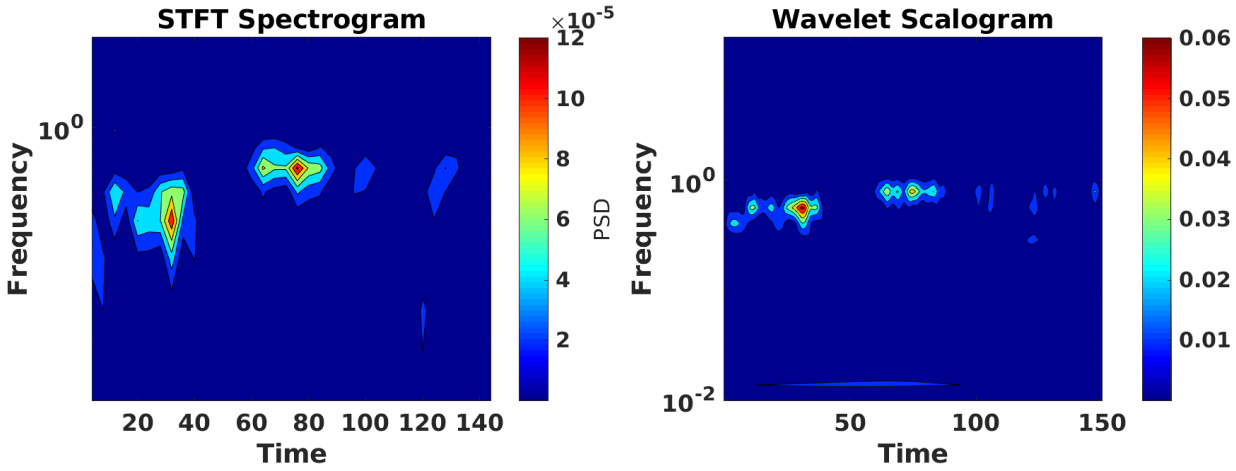

LIP1_5:

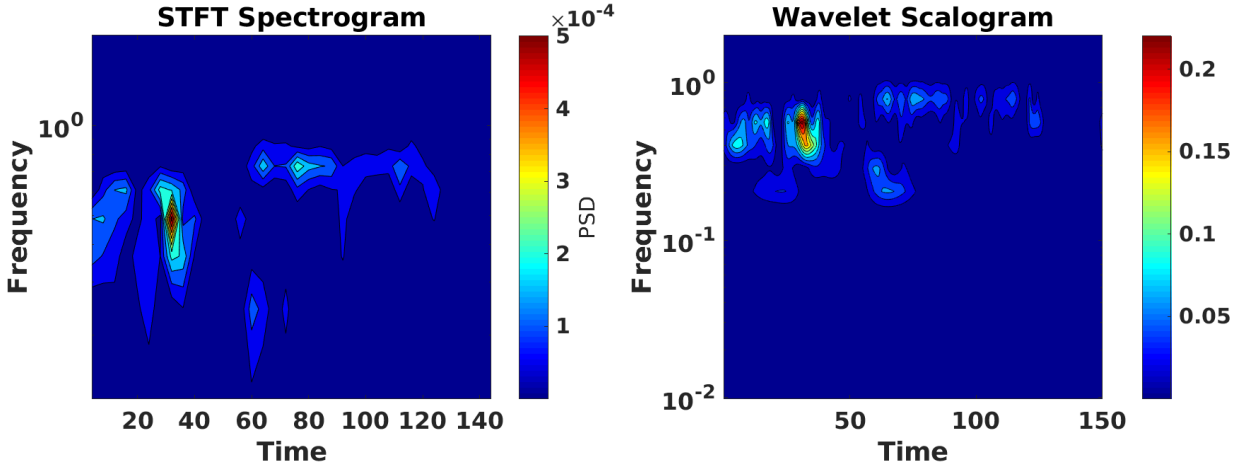

LIP1_6:

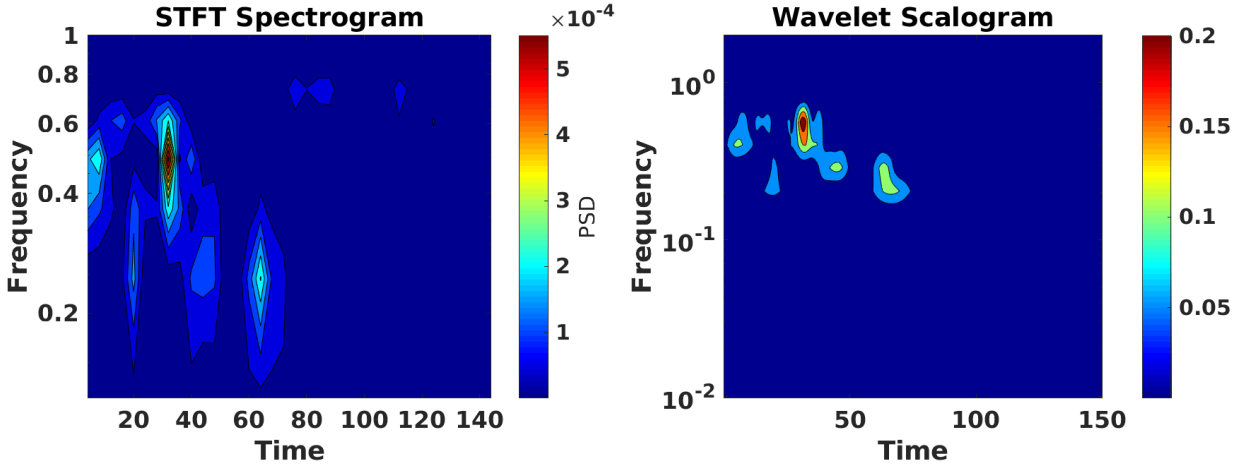

LIP1_7:

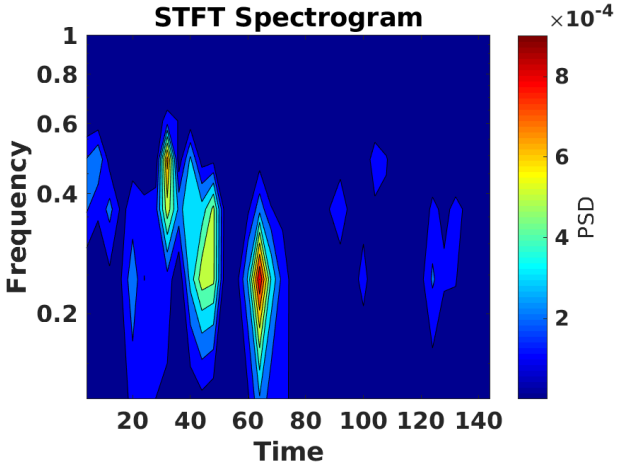

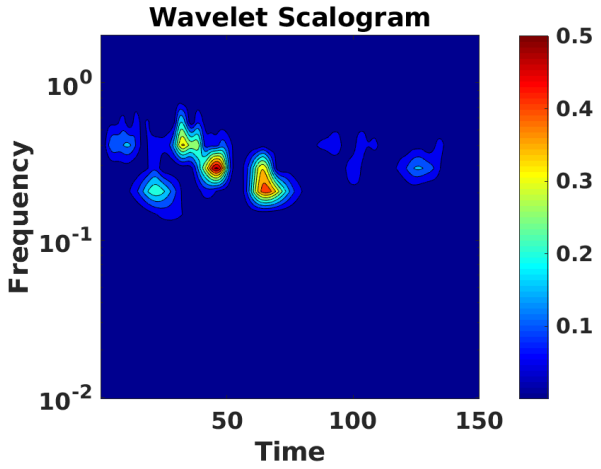

LIP1_8:

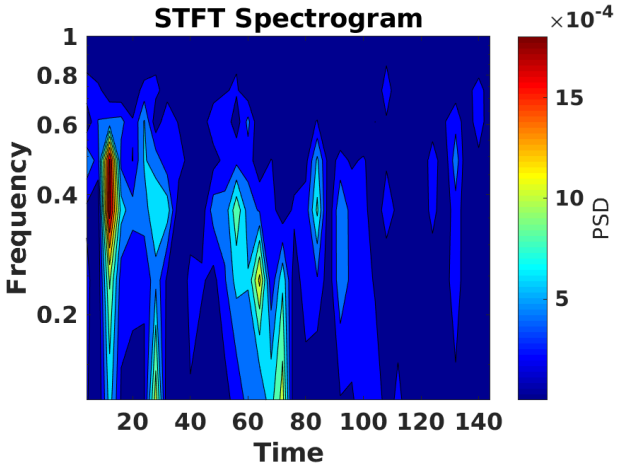

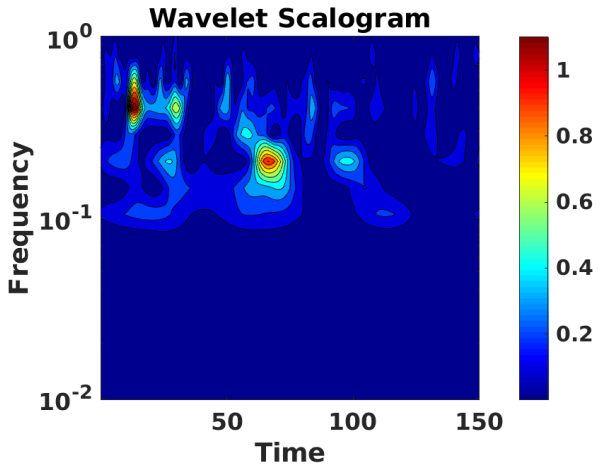

LIP2_2:

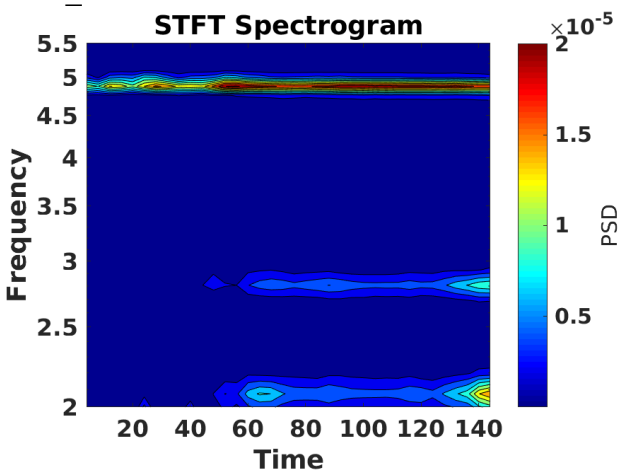

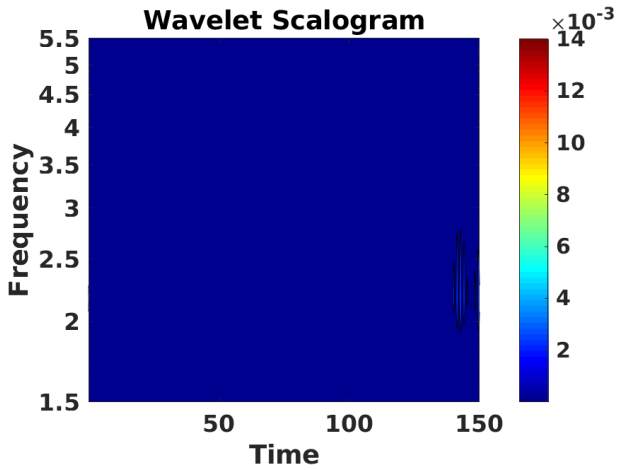

LIP2_3:

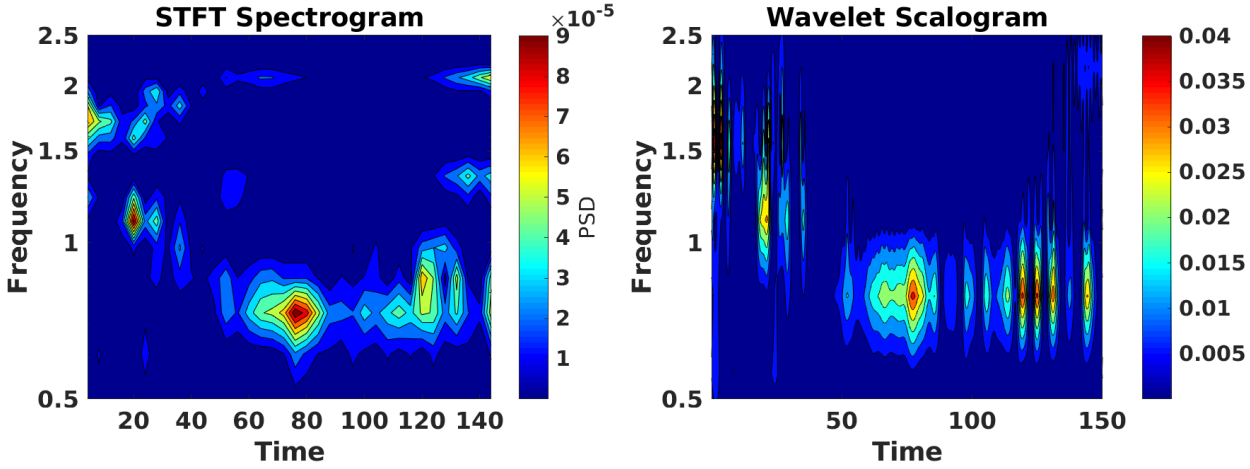

LIP2_4:

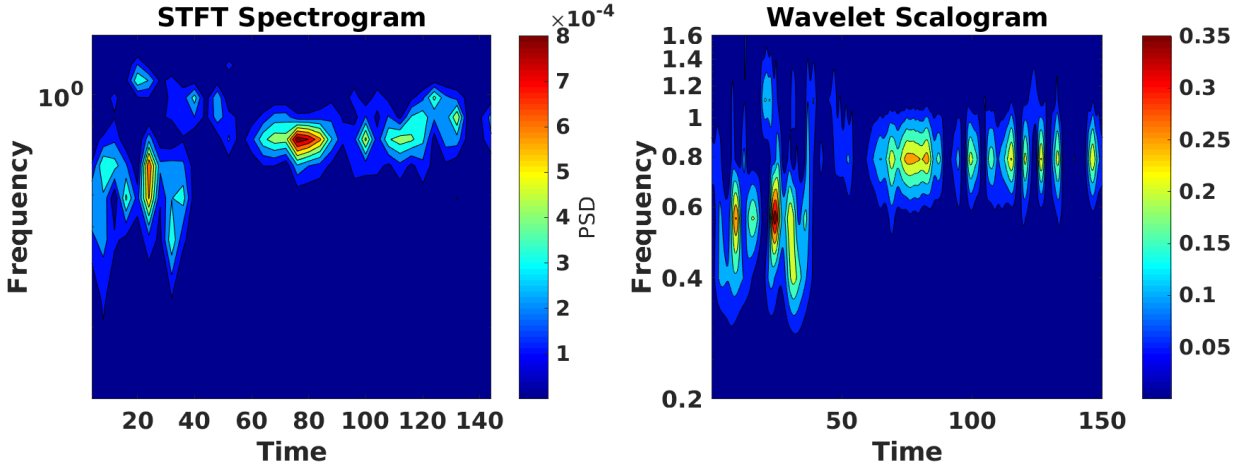

LIP2_5:

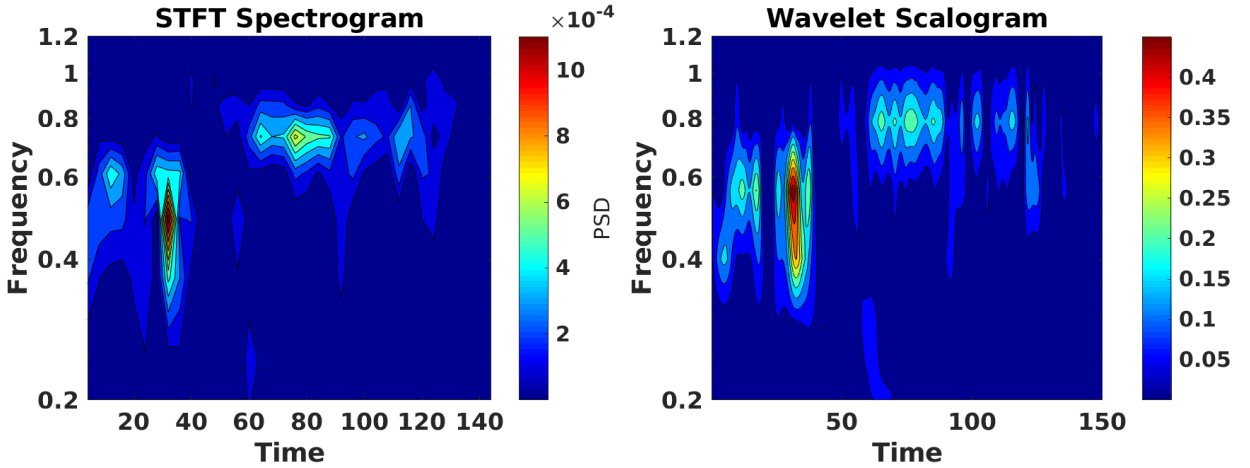

LIP2_6:

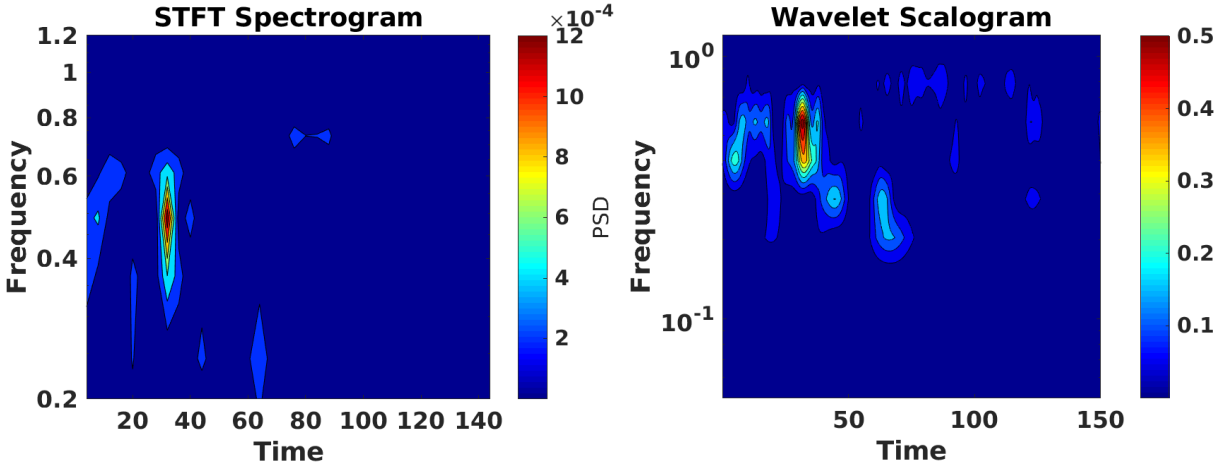

LIP2_7:

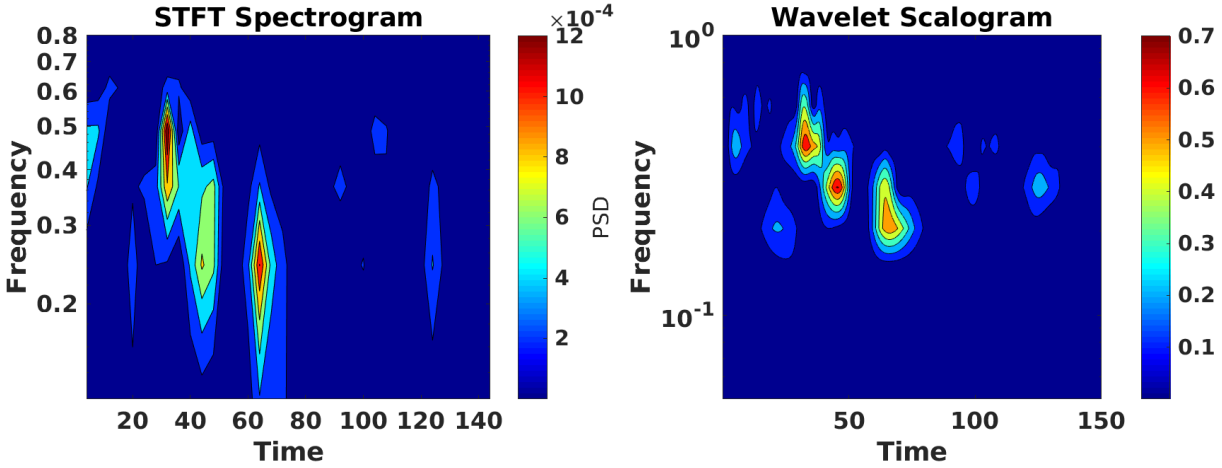

LIP2_8:

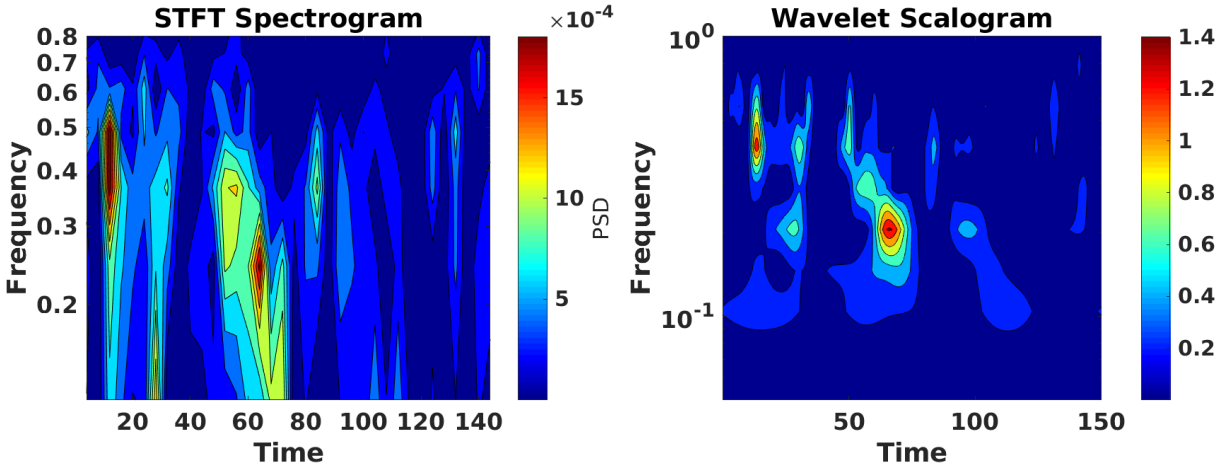

LIP3_1:

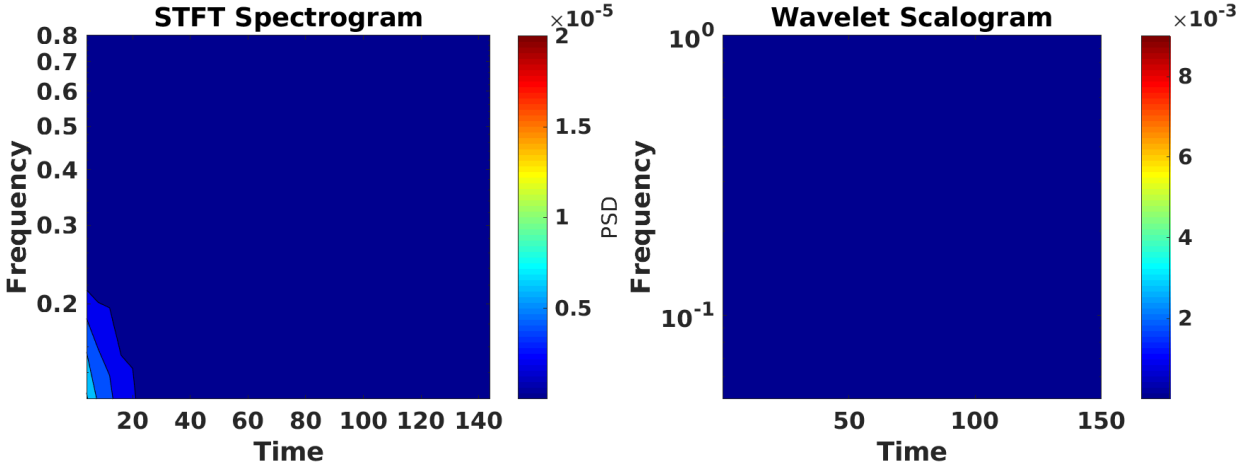

LIP3_2:

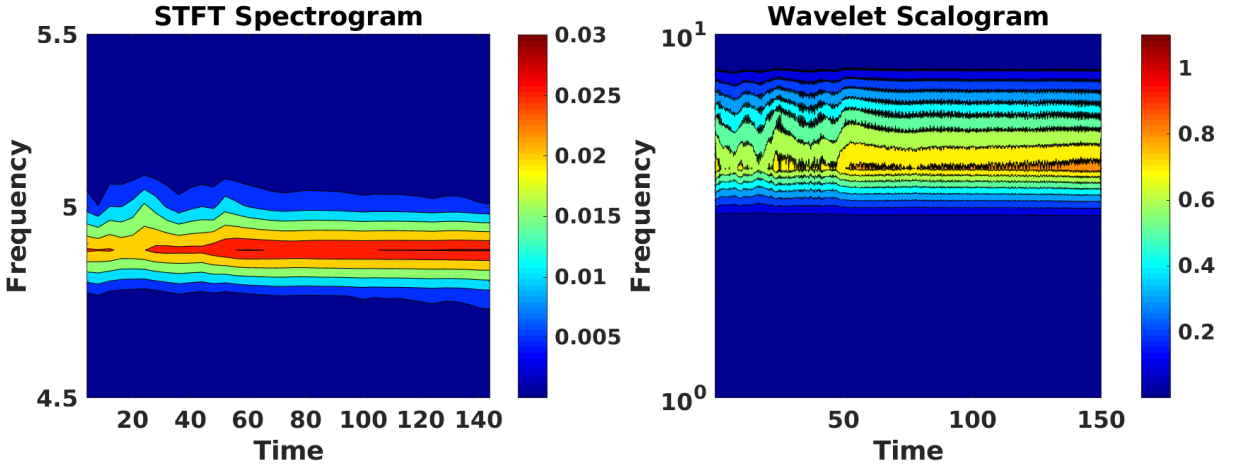

LIP3_3:

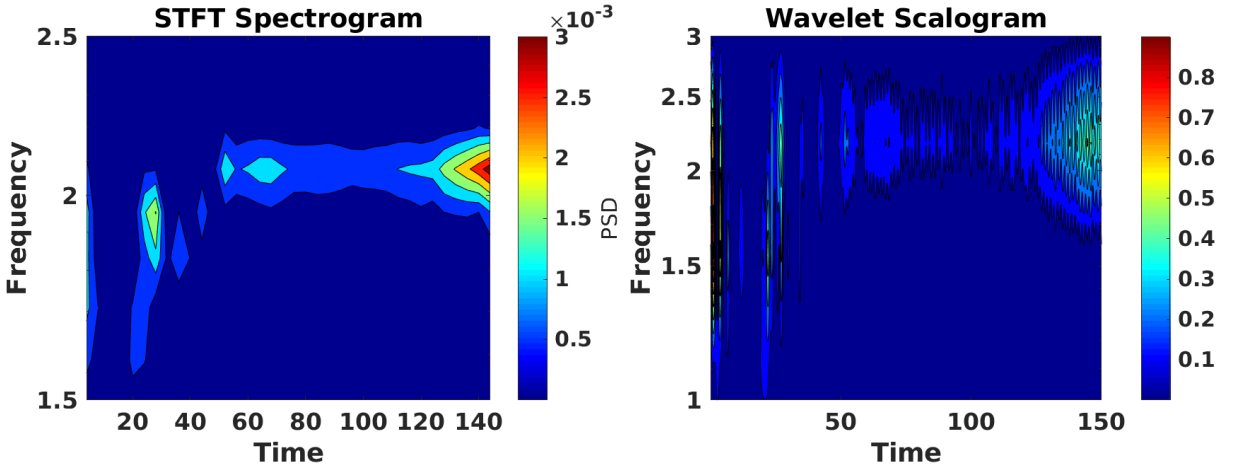

LIP3_4:

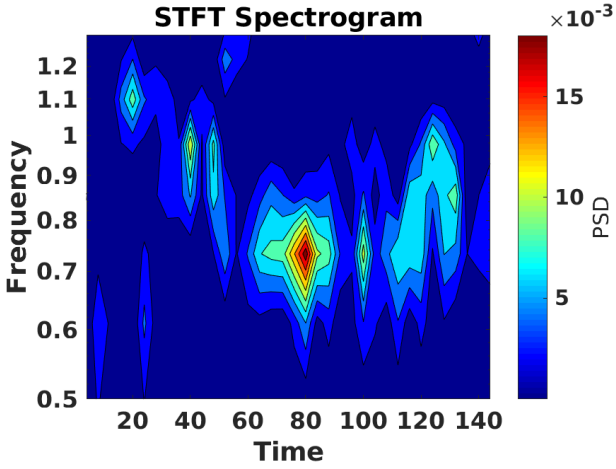

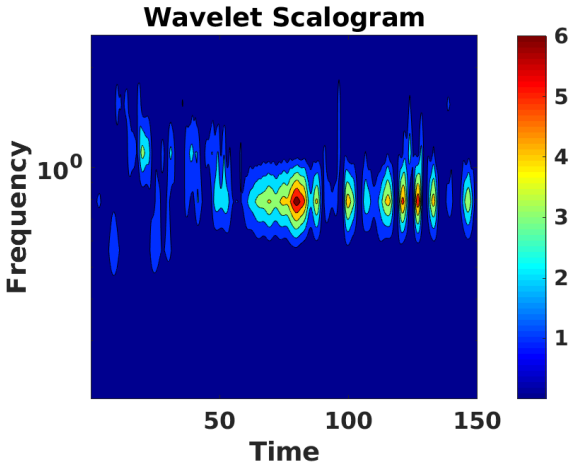

LIP3_5:

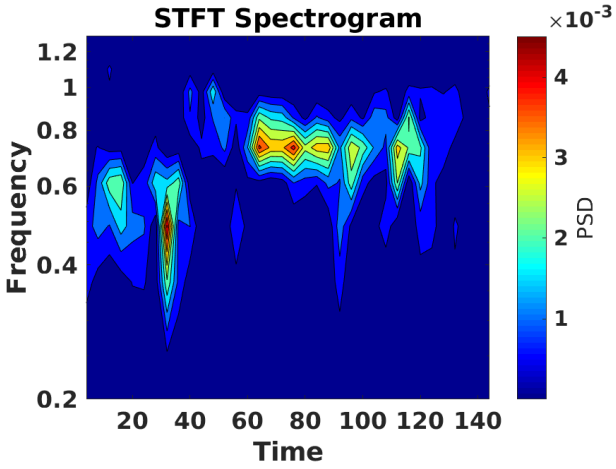

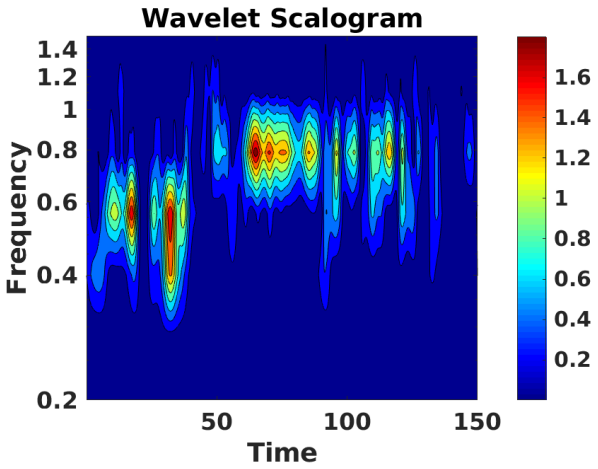

LIP3_6:

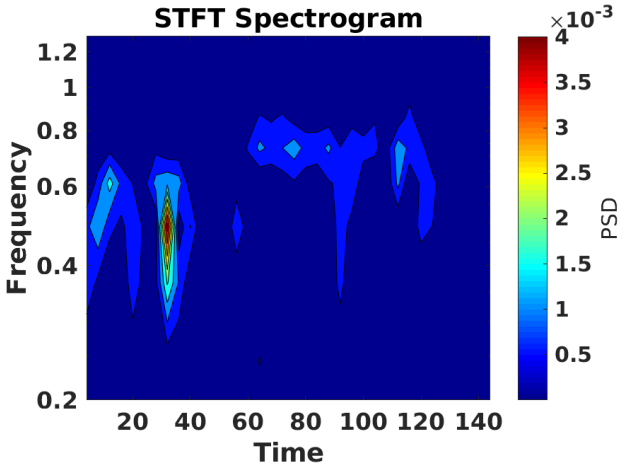

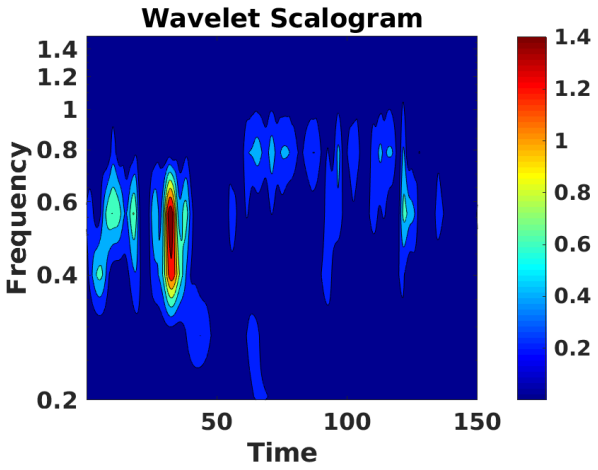

LIP3_7:

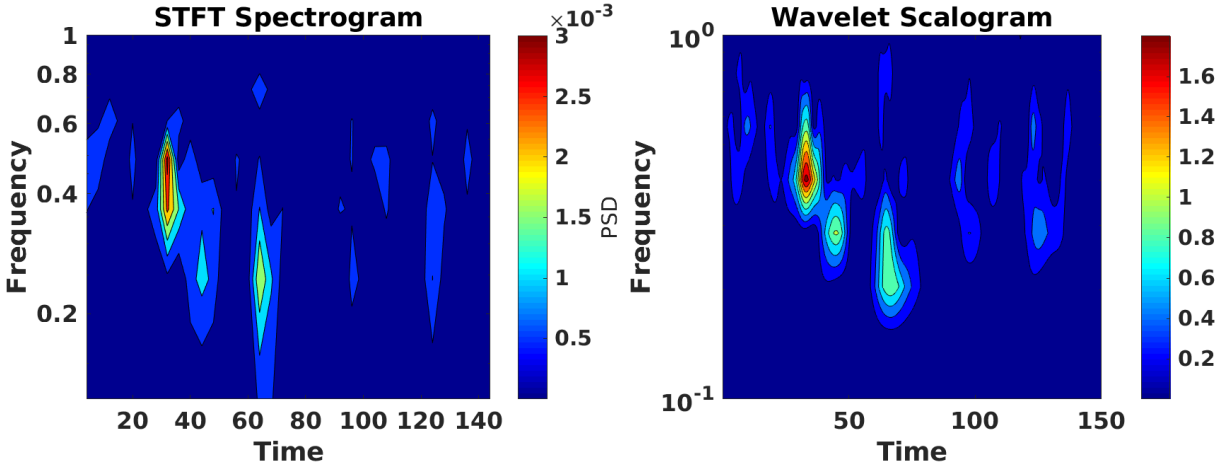
STFT Spectrogram
Frequency
Time
PSD
×10^-3
Wavelet Scalogram
Frequency
Time

LIP3_8:

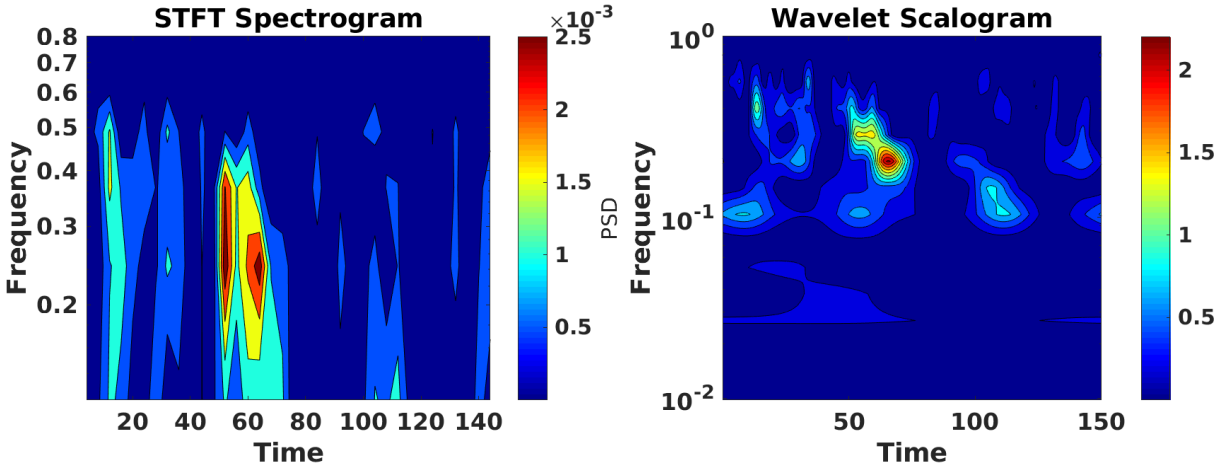
STFT Spectrogram
Frequency
Time
PSD
×10^-3
Wavelet Scalogram
Frequency
Time

Appendix C (matlab scripts used)

Fast Fourier Transform script:

```
%%%%%%%%%% Section plots p and p' for a given point data file%%%%%%%%%%%%
close all
clear all
clc
%%
data=dlmread('LIP3_8','',1,0);
time=data(:,1);
signal_one=data(:,5);
signal_two=data(:,5)-mean(data(:,5));

%% graph for 4999H presentation (just raw pressure data)
figure(1)
plot(time,signal_one)
title('Pressure VS Time at Point Probe','fontweight','bold','FontSize',18)
xlabel ('Time','fontweight','bold','FontSize',18)
ylabel ('p','fontweight','bold','FontSize',18)
xlim ([min(time) max(time)])
ylim ([min(signal_one) max(signal_one)])
print('LIP38_pressure','-dpng') % saves as png

%%
%%%%%%%%%%%%% section to compute FFT of p' and plot in terms of PSD%%%%%%
dt=0.001;    %to dimensionalize the data use uref and lref
Fs=1/dt;

NN = length(signal_two)
sig1=signal_two;
NFFT = 2^nextpow2(NN);
fftval=fft(sig1,NFFT);
fftval=abs(fftval).^2;
fftval=(1/(Fs*NN))*fftval;
fftval=2*fftval;
fftval=(fftval);
fftvalo=fftval(1:NFFT/2+1);
f1 = Fs/2*linspace(0,1,NFFT/2+1);
figure(2)
loglog(f1,fftvalo,'r','Linewidth',1.5)
grid on
% xlim ([0.01 50])
xlabel ('St','fontweight','bold','FontSize',18)
ylabel ('PSD','fontweight','bold','FontSize',18)
title ('PSD of pressure perturbation','fontweight','bold','FontSize',18)
print('LIP38_psd','-dpng') % saves as png


%%
%%%%% Section shows smoothing of the above PSD plot using Matlab smooth
%%%%% and Pwelch smoothing techniques%%%%%%%%%%%%%%%%%%%%%%%%%%%%%%%%%%%
% sit=3;
% fftvals=fftvalo;
% for it=1:1:sit
%     fftvals=smooth(fftvals);
```

```
% end

%%%%%%%%%%%%%%%%%%%%%%%%%%%%%%%%%%%%%%%%%%%%%%%%%%%%%%%%%%%%
%PWELCH PSD
NN = length(signal_two)
window=ceil(NN/12);
noverlap=ceil(window/2);
nfft = 2^nextpow2(window);
fs=Fs;
[pxx,f2] = pwelch(signal_two,window,noverlap,nfft,fs);


%%%%%%%%%%% Section to calculate SPL and OASPL %%%%%%%%%%%%%%%%%%%%%%%%%%
uref=347.1887;
rho_ref=1.1768;
p1=signal_one*rho_ref*uref*uref; % To convert non-dim pressure to dim
pressure
lref=0.095; %Reference length scale
t=time;
p1=p1-mean(p1);
pref=20*10^(-6);
p1=p1/pref;
dt=t(2)-t(1);
fs=1/dt;

N=length(p1);
nfft=2^nextpow2(N);
k=fft(p1,nfft);
freq=(fs/2)*linspace(0,1,nfft/2+1);
%freq = freq*0.053848/78.02;
k=abs(k).^2/(fs*N);
k1=k(1:nfft/2+1);
k1(2:end-1)=2*k1(2:end-1);
spl=10*log10(k1);

int=trapz(freq,k1(1:nfft/2+1));
oaspl1=10*log10(int);

%% Plot for 4999H presentation

figure (3)
semilogx(freq,spl,'r','Linewidth',2)
grid on
xlabel('St. Number','fontweight','bold','FontSize',18)
ylabel('SPL (dB)','fontweight','bold','FontSize',18)
title('SPL Profile at Point Probe','fontweight','bold','FontSize',18)
print('LIP38_spl','-dpng') % saves as png
```

Short-time Fourier Transform script:

```
close all
clear all
clc

data=dlmread('LIP3_8','',1,0);
t=data(:,1);
```

```
k=data(:,5)-mean(data(:,5));
N=length(k);
dt=0.001;
fs=1/dt;
%clev=linspace(0.00001,.0001,10);

%% PSD using FFT
nfft=2^nextpow2(N);
k_fft=abs(fft(k)).^2;
k_fft=k_fft/(fs*N);
k_fft=2*k_fft;
freq=(fs/2)*linspace(0,1,nfft/2+1);
figure(1)
semilogx(freq,k_fft(1:nfft/2+1),'LineWidth',2);
xlabel('Frequency','Fontweight','bold','Fontsize',16)
ylabel('PSD','Fontweight','bold','Fontsize',16)
title('Spectral distribution','Fontweight','bold','Fontsize',18)
set(gca,'fontweight','bold','FontSize',16)
xlim([0 5])
%% PSD using STFT
L=8000; %Window size
nfft=2^nextpow2(L);
[S,F,T,P]=spectrogram(k,L,L/2,nfft,(1/dt));
figure(2)
contourf(T,F,(abs(P)));
colormap jet
h=colorbar;
xlabel(h,'PSD')
axis tight;
view(0,90);
set(gca,'yscale','log');
xlabel('Time','Fontweight','bold','Fontsize',16)
ylabel('Frequency','Fontweight','bold','Fontsize',16)
title('STFT Spectrogram','Fontweight','bold','Fontsize',18)
set(gca,'fontweight','bold','FontSize',16)
ylim([0 .8])
print('-f2','LIP38_stft','-dpng') % saves as png
```

Wavelet Transform script:

```
close all
clear all
clc

data=dlmread('LIP3_8','',1,0);
t=data(:,1);
t=t-180;
k=data(:,5)-mean(data(:,5));
N=length(k);
dt=0.001;
fs=1/dt;
%clev=linspace(0.01,0.1,10);

%% PSD using FFT
nfft=2^nextpow2(N);
k_fft=abs(fft(k)).^2;
k_fft=k_fft/(fs*N);
```

```
k_fft=2*k_fft;
freq=(fs/2)*linspace(0,1,nfft/2+1);
figure(1)
semilogx(freq,k_fft(1:nfft/2+1),'LineWidth',2);
xlabel('Frequency','Fontweight','bold','Fontsize',16)
ylabel('Amplitude','Fontweight','bold','Fontsize',16)
title('Spectral distribution','Fontweight','bold','Fontsize',18)
set(gca,'fontweight','bold','FontSize',16)
xlim([0 5])

%%
ft=k;
sig={ft,dt};
cwtstruct = cwtft(sig);
cmag=(abs(cwtstruct.cfs).^2);
scales = cwtstruct.scales;
MorletFourierFactor = 4*pi/(6+sqrt(2+6^2));
freq = 1./(scales.*MorletFourierFactor);
figure(2)
contourf(t,freq,cmag);
colorbar
set(gca,'yscale','log');
ylim([0 1])
colormap jet
xlabel('Time','Fontweight','bold','Fontsize',16)
ylabel('Frequency','Fontweight','bold','Fontsize',16)
title('Wavelet Scalogram','Fontweight','bold','Fontsize',18)
set(gca,'fontweight','bold','FontSize',16)
print('-f2','LIP38_wavelet','-dpng') % saves as png
```

Appendix D (point probe locations)

File Name – IJK coordinates, XYZ coordinates
LIP1_4 – 300 169 53, -0.140676E+01 -0.670980E+00 -0.170568E-14
LIP1_5 – 350 169 53, -0.427580E+00 -0.393517E+00 -0.100035E-14
LIP1_6 – 425 169 53, 0.126672E+00 -0.271580E+00 -0.690376E-15
LIP1_7 – 501 169 53, 0.113908E+01 -0.268389E+00 -0.682265E-15
LIP1_8 – 575 169 53, 0.692291E+01 -0.274214E+00 -0.697071E-15
LIP2_2 – 200 299 53, -0.326918E+01 -0.123911E+01 -0.314992E-14
LIP2_3 – 225 299 53, -0.267323E+01 -0.109563E+01 -0.278517E-14
LIP2_4 – 275 299 53, -0.151827E+01 -0.810920E+00 -0.206142E-14
LIP2_5 – 350 299 53, -0.427625E+00 -0.505350E+00 -0.128464E-14
LIP2_6 – 425 299 53, 0.126672E+00 -0.384496E+00 -0.977416E-15
LIP2_7 – 501 299 53, 0.113908E+01 -0.381798E+00 -0.970559E-15
LIP2_8 – 575 299 53, 0.692291E+01 -0.390084E+00 -0.991621E-15
LIP3_1 – 125 399 53, -0.393786E+01 -0.152959E+01 -0.388832E-14
LIP3_2 – 175 399 53, -0.339611E+01 -0.136044E+01 -0.345833E-14
LIP3_3 – 225 399 53, -0.267324E+01 -0.123899E+01 -0.314961E-14
LIP3_4 – 275 399 53, -0.151827E+01 -0.104224E+01 -0.264945E-14
LIP3_5 – 350 399 53, -0.427720E+00 -0.743549E+00 -0.189015E-14
LIP3_6 – 425 399 53, 0.126672E+00 -0.625304E+00 -0.158957E-14
LIP3_7 – 501 399 53, 0.113908E+01 -0.625607E+00 -0.159034E-14
LIP3_8 – 575 399 53, 0.692291E+01 -0.639184E+00 -0.162485E-14